

REPORT DOCUMENTATION PAGE			Form Approved OMB NO. 0704-0188	
Public Reporting burden for this collection of information is estimated to average 1 hour per response, including the time for reviewing instructions, searching existing data sources, gathering and maintaining the data needed, and completing and reviewing the collection of information. Send comment regarding this burden estimates or any other aspect of this collection of information, including suggestions for reducing this burden, to Washington Headquarters Services, Directorate for information Operations and Reports, 1215 Jefferson Davis Highway, Suite 1204, Arlington, VA 22202-4302, and to the Office of Management and Budget, Paperwork Reduction Project (0704-0188,) Washington, DC 20503.				
1. AGENCY USE ONLY (Leave Blank)		2. REPORT DATE		3. REPORT TYPE AND DATES COVERED
4. TITLE AND SUBTITLE			5. FUNDING NUMBERS	
6. AUTHOR(S)				
7. PERFORMING ORGANIZATION NAME(S) AND ADDRESS(ES)			8. PERFORMING ORGANIZATION REPORT NUMBER	
9. SPONSORING / MONITORING AGENCY NAME(S) AND ADDRESS(ES) U. S. Army Research Office P.O. Box 12211 Research Triangle Park, NC 27709-2211			10. SPONSORING / MONITORING AGENCY REPORT NUMBER	
11. SUPPLEMENTARY NOTES The views, opinions and/or findings contained in this report are those of the author(s) and should not be construed as an official Department of the Army position, policy or decision, unless so designated by other documentation.				
12 a. DISTRIBUTION / AVAILABILITY STATEMENT Approved for public release; distribution unlimited.			12 b. DISTRIBUTION CODE	
13. ABSTRACT (Maximum 200 words)				
14. SUBJECT TERMS			15. NUMBER OF PAGES	
			16. PRICE CODE	
17. SECURITY CLASSIFICATION OR REPORT UNCLASSIFIED	18. SECURITY CLASSIFICATION ON THIS PAGE UNCLASSIFIED	19. SECURITY CLASSIFICATION OF ABSTRACT UNCLASSIFIED	20. LIMITATION OF ABSTRACT UL	

NSN 7540-01-280-5500

Standard Form 298 (Rev.2-89)
Prescribed by ANSI Std. Z39-18
298-102

Enclosure 1

Simulation of Transient Dynamics of Shock Wave Boundary Layer Interactions using Hybrid Large-Eddy / Reynolds-Averaged Navier-Stokes Models

Final Technical Report

**Army Research Office
Short Term Innovative Research Grant
W911NF-06-1-0299**

Submitted by

**Dr. Jack R. Edwards
Department of Mechanical and Aerospace Engineering
Campus Box 7910
North Carolina State University
Raleigh, NC 27695**

To

**Department of the Army
U.S. Army Research, Development and Engineering Command Acquisition
Center
(Attn. Dr. Thomas Doligalski, ARO Grants Representative)
Research Triangle Park Contracting Division
P.O. Box 12211
Research Triangle Park, North Carolina, 27709-2211**

TABLE OF CONTENTS

<u>Section</u>	<u>Page Numbers</u>
Table of Contents	2
Project Abstract (Original Proposal)	3
1. Background and Objectives	4-5
2. Numerical Methods	5-6
3. Turbulence Models	6-10
3.1. Menter's SST Model	6-7
3.2. Hybrid LES/RANS Extension	7-9
3.3. Recycling / Rescaling Method	9-10
4. Calculation Details	10-12
4.1. Test Geometry and Boundary Conditions	
4.2. Initialization Procedure and Time Evolution Details	11-12
5. Results and Discussion	12-35
5.1. Flat Plate Boundary Layer	12-14
5.2. Three Dimensional Flow Structure	14-21
5.3. Comparisons with Experimental Mean Flow Data	21-26
5.4. Dynamics of Shock-System Motion	26-30
5.5. Comparisons with RANS Mean Flow Data	30-33
5.6. Comparisons with RANS Reynolds Stress Data	33-35
6. Conclusions	35-37
7. Directions for Future Work	37
Publications	38
Personnel	38
Bibliography	38-40
Appendices	40

Project Abstract (Original Proposal)

Many experimental investigations have noted that complex shock / boundary layer interactions exhibit large-scale, low frequency motion that is distinct from that associated from wall-layer turbulence. This motion results in fluctuating pressure and heat-transfer loads that can adversely affect the performance of supersonic missile systems, among others. Accurate predictions of such effects would appear to require a time-dependent modeling strategy, such as large-eddy simulation (LES) or direct numerical simulation (DNS). The application of these techniques to flows at practical Reynolds numbers requires immense computational resources, and as yet, very few studies have provided one-to-one comparisons with experimental data. A promising alternative to traditional LES/DNS are hybrid large-eddy / Reynolds-averaged Navier-Stokes (LES/RANS) models, which essentially function as a large-eddy simulation away from solid surfaces but revert to a RANS-based closure near solid surfaces. Recent simulations of two- and three-dimensional shock / boundary layer interactions using a class of “zonal” LES/RANS methods developed at North Carolina State University have shown that these techniques can predict time-averaged flow field properties as well as or better than RANS models. The techniques naturally capture both large-scale and small-scale flow features, but an open question is whether the dynamics of the shock / boundary layer interactions is predicted correctly. This tightly focused research effort will attempt to answer this question by conducting detailed hybrid LES/RANS simulations of the Mach 5, 28 degree compression-corner flows studied by David Dolling’s group at the University of Texas. This data is the most comprehensive set available for studying shock interaction dynamics and includes conditionally-averaged pitot and static pressure distributions, wavelength, amplitude, and frequency information associated with the shock structure, and cross-correlation analyses. Simulations will be conducted for this interaction and will involve investigation of the effects of variations in the turbulence modeling parameters, the extent of the computational domain, and the degree of mesh refinement on the predictions. Data extraction will mimic that used in the experimental measurements (to the extent possible). This will enable the one-to-one, time-resolved comparisons necessary for a complete assessment. Results obtained through a successful validation should provide directions for improvement in less-expensive, lower-fidelity models (unsteady RANS or very large eddy simulation (VLES)) and will perhaps yield new insights into the causes of large-scale unsteadiness in flows driven by shock / boundary layer interactions.

1. Background and Objectives

The accurate prediction of high-speed flows can depend critically on the ability of the chosen model to account for shock wave / boundary layer interactions. For example, off-design aerodynamic performance of missiles can be affected by shock / boundary layer interactions induced by plume interference, and the initial stages of launch for many ballistics concepts involve multiple shock / boundary layer interactions. Maneuvering of launched missiles may involve movement of fins or control surfaces, which could also result in shock / boundary layer interactions. A clear understanding of the effects of the associated fluctuating pressure and heating loads is necessary to better refine control techniques, to predict failure scenarios, and to determine ranges of efficient operation. A complicating factor in many shock wave / boundary layer interactions is a degree of global flowfield unsteadiness, apart from that due to turbulent fluctuations, that can dominate the response. The work of David Dolling and his colleagues [1-8], spanning nearly twenty years, has provided the most complete characterization of the dynamics of shock / boundary layer interactions. The database includes conditionally-averaged pitot and static pressure distributions (conditioned on the separation shock position), wavelength, amplitude, and frequency information associated with the shock structure, and cross-correlation analyses designed to elucidate the underlying causes of the global motion. Trends revealed during this study raise serious concerns about the ability of traditional Reynolds-averaging techniques to predict shock / boundary layer interactions and appear to indicate that time-accurate, three-dimensional modeling strategies (such as DNS or LES) may be required for precision.

The objective of the current work is to apply a hybrid LES/RANS framework developed at NCSU [9-13] to the Dolling Mach 5 compression-corner configuration to determine the model's ability to capture the time-dependent structure of this flow. The viewpoint taken in the NCSU model is that the RANS component functions as a form of near-wall closure in an otherwise LES description of the flow. A strong coupling of the model response with the boundary layer structure is therefore required, and this is facilitated first by the design of a RANS-to-LES transition function that is based on the modeled structure of the flow in the logarithmic region and second, by the use of "recycling / re-scaling" techniques that sustain the transport of large turbulent structures in the outer part of the boundary layer. While predictions of mean-flow properties have been evaluated in earlier works [9-13], this study also focuses on the prediction of second-moment quantities and on the dynamics of the shock / boundary layer interaction. In this scope and in its one-to-one comparisons with available experimental data at the same conditions, the present work is closely related to the Mach 3 LES investigation of flow over a compression corner conducted by Loginov, et al [14], the Mach 3 DNS compression-corner calculations of Wu and Martin [15], and the earlier "very" large-eddy simulations of Mach 3 flow over a compression corner of Hunt and Nixon [16]. Both the Loginov, et al. and Wu and Martin investigations used over 18 million mesh points in their calculations. Because of the near-wall modeling in our hybrid LES/RANS approach, we can reduce the resolution requirements significantly and can compute flows at even higher Reynolds numbers. It will be shown that many of the features of the Dolling-group compression corner experiments are captured to a good degree of precision by the hybrid LES/RANS model. The remainder of this report outlines the numerical methods used (Section 2), the turbulence closure models (Section 3), and other calculation details (Section 4). The results of the investigation are presented in

Section 5, some conclusions are outlined in Section 6, and directions for future work are presented in Section 7.

2. Numerical Methods

Simulations were performed using NCSU's REACTMB code [17]. In REACTMB, the governing equations are discretized in a finite-volume manner. Inviscid fluxes are discretized using Edwards' LDFSS scheme [18], while viscous and diffusive fluxes are discretized using second-order central differences. The LDFSS scheme is extended to second or higher-order spatial accuracy using the piecewise parabolic method (PPM) [19], as described later. A dual-time stepping implicit method is used to advance the equations in time. At each time step, a Crank-Nicholson discretization of the equations is solved to a prescribed tolerance using a sub-iteration procedure. The matrix system resulting from the linearization of the equation system is approximately solved using a planar relaxation procedure at each sub-iteration. To enhance computational efficiency, matrix elements are evaluated and factored every second time step and are held fixed over the duration of the sub-iterations.

In an effort to enhance the ability of REACTMB to capture fine-scale structures, the Sonic-A ENO scheme [20] used in our prior work has been replaced by a version of the classic piecewise parabolic method (PPM) [19]. In contrast to the ENO schemes described in [20] and to the standard forms of weighted-ENO (WENO) schemes, the PPM reduces to a fourth-order central differencing scheme for sufficiently smooth data, enhancing its ability to capture high-frequency features. A cell-by-cell limiting procedure reduces the order of accuracy in the vicinity of local extrema in the solution. A general interface flux formula may be written as $\vec{F}_{i+1/2}(\vec{V}_{L,i+1/2}, \vec{V}_{R,i+1/2})$, with left-and-right state interpolations $\vec{V}_{L,i+1/2}$ and $\vec{V}_{R,i+1/2}$ determined by the step-by-step procedure described below.

Step 1: initially set left-and-right state values to fourth-order averaging operators. If unmodified, these provide a fourth-order central difference approximation to the flux difference $\vec{F}_{i+1/2} - \vec{F}_{i-1/2}$:

$$\vec{V}_{L,i+1/2} = \vec{V}_{R,i+1/2} = \frac{7}{2}(\vec{V}_i + \vec{V}_{i+1}) - \frac{1}{12}(\vec{V}_{i+2} + \vec{V}_{i-1}) \quad (1)$$

Step 2: conduct cell-by-cell limiting to enforce monotonicity:

$$\begin{aligned}
& \text{if } \text{sgn}[(\vec{V}_{L,i+1/2} - \vec{V}_i)(\vec{V}_i - \vec{V}_{R,i-1/2})] = -1, \text{ then} \\
& \quad \vec{V}_{L,i+1/2} = \vec{V}_{R,i-1/2} = \vec{V}_i \\
& \text{else} \\
& \quad C = \vec{V}_{L,i+1/2} - \vec{V}_{R,i-1/2} \\
& \quad D = 6.0[\vec{V}_i - \frac{1}{2}(\vec{V}_{L,i+1/2} + \vec{V}_{R,i-1/2})] \\
& \quad \text{if}(DC > CC) \text{ then} \\
& \quad \quad \vec{V}_{R,i-1/2} = 3\vec{V}_i - 2\vec{V}_{L,i+1/2} \\
& \quad \text{elseif}(-CC > DC) \text{ then} \\
& \quad \quad \vec{V}_{L,i+1/2} = 3\vec{V}_i - 2\vec{V}_{R,i-1/2} \\
& \quad \text{end if} \\
& \text{end if}
\end{aligned} \tag{2}$$

The first ‘if’ block resets the interpolation function to a constant if \vec{V}_i is a local maximum or minimum. The second ‘if’ block resets either the left-state value at interface $i + 1/2$ or the right-state value at interface $i - 1/2$ so that the interpolation parabola that connects the interface states with the state at the cell center is monotonically increasing or decreasing. It is also possible to enforce physical constraints (such as positive temperatures, densities, and mass fractions) at the cell interfaces by a similar cell-by-cell resetting algorithm. The PPM requires a seven point stencil in each coordinate direction, and the reconstruction procedures are applied to the primitive-variable vector $\vec{V} = [\rho, u, v, w, T, k, \omega]^T$.

3. Turbulence Closure

3.1. Menter’s SST Model

The RANS turbulence model used in this investigation is Menter’s hybrid $k - \omega / k - \varepsilon$ shear-stress transport (SST) model.[21] The transport equations for the turbulence kinetic energy, k , and the specific dissipation rate, ω for Menter’s model are given by

$$\frac{\partial(\rho k)}{\partial t} + \frac{\partial(\rho k u_j)}{\partial x_j} = \mu_t S^2 - \beta^* \rho \omega k + \frac{\partial}{\partial x_j} \left[(\mu + \sigma_k \mu_t) \frac{\partial k}{\partial x_j} \right] \tag{3}$$

$$\frac{\partial(\rho \omega)}{\partial t} + \frac{\partial(\rho \omega u_j)}{\partial x_j} = \gamma \rho S^2 - \beta \rho \omega^2 + \frac{\partial}{\partial x_j} \left[(\mu + \sigma_\omega \mu_t) \frac{\partial \omega}{\partial x_j} \right] + 2(1 - F_1) \rho \sigma_{\omega 2} \frac{1}{\omega} \frac{\partial k}{\partial x_j} \frac{\partial \omega}{\partial x_j} \tag{4}$$

where S is defined as

$$S = \left[\frac{\partial \tilde{u}_i}{\partial x_j} \frac{\partial \tilde{u}_j}{\partial x_i} + \frac{\partial \tilde{u}_i}{\partial x_j} \frac{\partial \tilde{u}_j}{\partial x_i} - \frac{2}{3} \left(\frac{\partial \tilde{u}_i}{\partial x_i} \right)^2 \right]^{1/2} \tag{5}$$

and ϕ represents any constant in Menter's model ($\sigma_k, \sigma_\omega, \dots$), averaged according to the blending function F_1

$$\phi = F_1 \phi_1 + (1 - F_1) \phi_2 \quad (6)$$

The ϕ_1 constants are from the $k - \omega$ model:

$$\begin{aligned} \sigma_{k1} &= 0.85, \sigma_{\omega1} = 0.5, \beta_1 = 0.075 \\ \beta^* &= 0.09, \kappa = 0.41, \gamma_1 = \frac{\beta_1}{\beta^*} - \frac{\sigma_{\omega1} \kappa^2}{\sqrt{\beta^*}} \end{aligned} \quad (7)$$

and the ϕ_2 constants are from the standard $k - \varepsilon$ model:

$$\begin{aligned} \sigma_{k2} &= 1.0, \sigma_{\omega2} = 0.856, \beta_2 = 0.0828 \\ \beta^* &= 0.09, \kappa = 0.41, \gamma_2 = \frac{\beta_2}{\beta^*} - \frac{\sigma_{\omega2} \kappa^2}{\sqrt{\beta^*}} \end{aligned} \quad (8)$$

The blending function F_1 is defined as

$$F_1 = \tanh(\arg_1^4), \arg_1 = \max\left(\frac{\sqrt{k}}{0.09\omega d}, \frac{500\nu}{d^2\omega}\right) \quad (9)$$

where d is the distance to the nearest wall. The eddy viscosity is defined as:

$$\nu_t = \frac{a_1 k}{\max(a_1 \omega, A_{sst} \Omega F_2)} \quad (10)$$

where $a_1 = 0.31$, Ω is the magnitude of the vorticity vector, and F_2 is another blending function given by

$$F_2 = \tanh(\arg_2^2), \arg_2 = \max\left(2 \frac{\sqrt{k}}{0.09\omega d}, \frac{500\nu}{d^2\omega}\right) \quad (11)$$

This 'shear stress transport' (SST) modification alters the turbulence frequency as used in the eddy viscosity definition in the vicinity of high strain rates. The general effect is to lower the eddy viscosity and thus to promote the growth of regions of separated flow. As shown later, the RANS predictions for Dolling's compression-corner experiments (and similar shock / boundary layer interactions) are sensitive to the constant A_{sst} in Eq. (9), which ranges between zero (for no SST modification) to one (for the full SST contribution).

3.2. Hybrid LES/RANS Extension

Several approaches have been used in our earlier work to extend Menter's model to serve as the RANS component of a hybrid LES/RANS closure [9-13]. In this investigation, we have opted for a simple strategy motivated by Strehlets' [22] development of a two-equation detached-eddy simulation method. The eddy viscosity as used in the turbulence transport equations and the main flow equations is defined as a weighted sum of a RANS description and a Smagorinsky model:

$$\mu_t = \rho \nu_t = \rho \left(\Gamma \frac{a_1 k}{\max(a_1 \omega, A_{sst} \Omega F_2)} + (1 - \Gamma) C_s \Delta^2 S \right), \Delta = (\Delta_x \Delta_y \Delta_z)^{1/3}, C_s = 0.01 \quad (12)$$

The blending function Γ is designed to shift the closure from a RANS description near solid surfaces to an LES description in the outer parts of the boundary layer and in regions of flow separation. The blending function is based on the ratio of the wall distance d to a modeled form of the Taylor micro-scale:

$$\Gamma = \frac{1}{2} \left(1 - \tanh \left[5 \left(\frac{\kappa}{\sqrt{C_\mu}} \eta^2 - 1 \right) - \phi \right] \right), \quad \eta = \frac{d}{\alpha_1 \chi} \quad (13)$$

with the Taylor micro-scale defined as

$$\lambda = \sqrt{\nu / C_\mu \omega} \quad (14)$$

The primary advantage of this form is that the location of the RANS/LES juncture (defined as $\Gamma=0.5$) can be correlated as a function of the wall coordinate $d^+ = u_\tau d / \nu$. Substituting the log-law expression for the turbulence frequency $\omega = u_\tau / (\sqrt{\beta_*} \kappa d)$ into (14) and placing the result in (13), it can be shown that the $\Gamma=0.5$ position should occur at $d^+ = \alpha_1^2$ if $\phi = 0.0$. The constant α_1 then can be used control the position of the juncture, assuming that the log-law scaling is maintained. The value of “5” in Eq. (13) controls the sharpness of the transition, and the constant ϕ can be used to shift the mid-point of the blending function. In this work, ϕ is set to 2.2975599, so that the balancing position (where $\frac{\kappa}{\sqrt{C_\mu}} \eta^2 = 1$) corresponds to $\Gamma=0.9$ instead of $\Gamma=0.5$.

To determine the constant α_1 for a particular inflow boundary layer, the following procedure is used. First, a prediction of the equilibrium boundary layer is obtained, given free-stream properties, a specified wall condition (adiabatic or isothermal) and a value for the boundary layer thickness (0.0175 m for the Dolling Mach 5 experiments), from Coles’ Law of the Wall / Wake along with the Van Driest transformation:

$$\frac{u_{vd}}{u_\tau} = \frac{1}{\kappa} \ln(d_w^+) + C + 2 \frac{\Pi}{\kappa} \sin^2 \left(\frac{\pi}{2} \frac{d}{\delta} \right), \quad d_w^+ = \frac{u_\tau d}{\nu_w} \quad (15)$$

with

$$u_{vd} = \frac{u_\infty}{A} \left\{ \sin^{-1} \left[\frac{2A^2 u / u_\infty - B}{\sqrt{B^2 + 4A^2}} \right] + \sin^{-1} \left[\frac{B}{\sqrt{B^2 + 4A^2}} \right] \right\}, \quad (16)$$

$$A = \sqrt{\frac{(\gamma-1)}{2} \text{Pr}_t M_\infty^2 \frac{T_\infty}{T_w}}, \quad B = \left[1 + \text{Pr}_t^{1/2} \frac{(\gamma-1)}{2} M_\infty^2 \right] \frac{T_\infty}{T_w} - 1$$

An initial estimate for the outer extent of the log layer is defined by finding the value of d_w^+ such

that $\left(\frac{1}{\kappa} \ln(d_w^+) + C \right) / \left(\frac{u_{vd}}{u_\tau} \right) = 0.98$. The value of $d^+ = u_\tau d / \nu$ that corresponds to this value of

d_w^+ is then found through the use of Walz’s formula for the static temperature distribution within the boundary layer [23]:

$$\frac{T}{T_\infty} = \frac{T_w}{T_\infty} + \frac{(T_{aw} - T_w)}{T_\infty} \frac{u}{u_\infty} - r \frac{(\gamma - 1)}{2} M_\infty^2 \left(\frac{u}{u_\infty} \right)^2 \quad (17)$$

Since the kinematic viscosity ν is a function of temperature, the target value for d^+ will differ significantly from d_w^+ for high Mach number flows. For the inflow boundary layer in the Mach 5 Dolling experiments, a value of $\alpha_1 = 42.042$ is calculated using this procedure.

A key to the blending function response is the relative insensitivity of the turbulence frequency to changes in the turbulence kinetic energy and the eddy viscosity. This means that the average location of the blending function (in terms of its distance from the wall) will not vary significantly. The dependence of the turbulence frequency on the local strain rate S means that the instantaneous position of the interface will vary in response to resolved-eddy dynamics. The calibration procedure described above is problem-dependent, and it is not clear as yet that the procedure is self-similar in that the $\Gamma = 0.5$ blending function position would recover to its target location if the initial equilibrium boundary layer relaxes to another equilibrium state. Efforts are underway to analyze the response of this technique (and other blending strategies) using RANS mean data.

3.3. Recycling-Re-scaling Method

A recycling / rescaling technique, applied to the fluctuating fields, is used to initiate and sustain turbulent structures. In this procedure, fluctuations in the fluid properties at a ‘recycle plane’ are extracted by subtracting the instantaneous profile from a time- and span-averaged profile. The fluctuation fields are then rescaled according to boundary layer similarity laws and superimposed onto a RANS mean inflow profile. The general procedure is described in [10] and [11]. One modification used in this work to prevent excessive turbulence energy accumulation in the outer part of the boundary layer is to multiply the recycled fluctuations by a Klebanoff-type intermittency function [24]:

$$\begin{aligned} q_{\text{inflow}} &= q_{\text{RANS}} + F_{\text{kleb}} q'_{\text{recyc}}; \quad q = \text{density, velocity, temperature} \\ q_{\text{inflow}} &= (1 - F_{\text{kleb}}) q_{\text{RANS}} + F_{\text{kleb}} q_{\text{recyc}}; \quad q = \text{turbulence variables} \\ F_{\text{kleb}} &= (1 + (d/C_{\text{kleb}} \delta)^6)^{-1} \end{aligned} \quad (18)$$

with $C_{\text{kleb}} = 1.10$. This procedure also ensures that the RANS free-stream inflow properties are not altered outside the boundary layer. In our prior work, we have assumed negligible pressure fluctuations to determine the fluctuations in density, given the fluctuations in temperature. We relax this assumption in this work in order to allow a user-specified pressure fluctuation level. We also require that the recycled temperature fluctuations be no greater (in magnitude) than allowed by Morkovin’s hypothesis of negligible total-temperature fluctuations. From Morkovin’s hypothesis,

$$\begin{aligned} C_p T'_{\text{mork}} &= -[F_{\text{kleb}} (u_{\text{RANS}} u'_{\text{recyc}} + v_{\text{RANS}} v'_{\text{recyc}} + w_{\text{RANS}} w'_{\text{recyc}}) + \\ &\quad \frac{1}{2} F_{\text{kleb}}^2 (u_{\text{recyc}}'^2 + v_{\text{recyc}}'^2 + w_{\text{recyc}}'^2)] \end{aligned} \quad (19)$$

and the recycled temperature fluctuation is limited as follows:

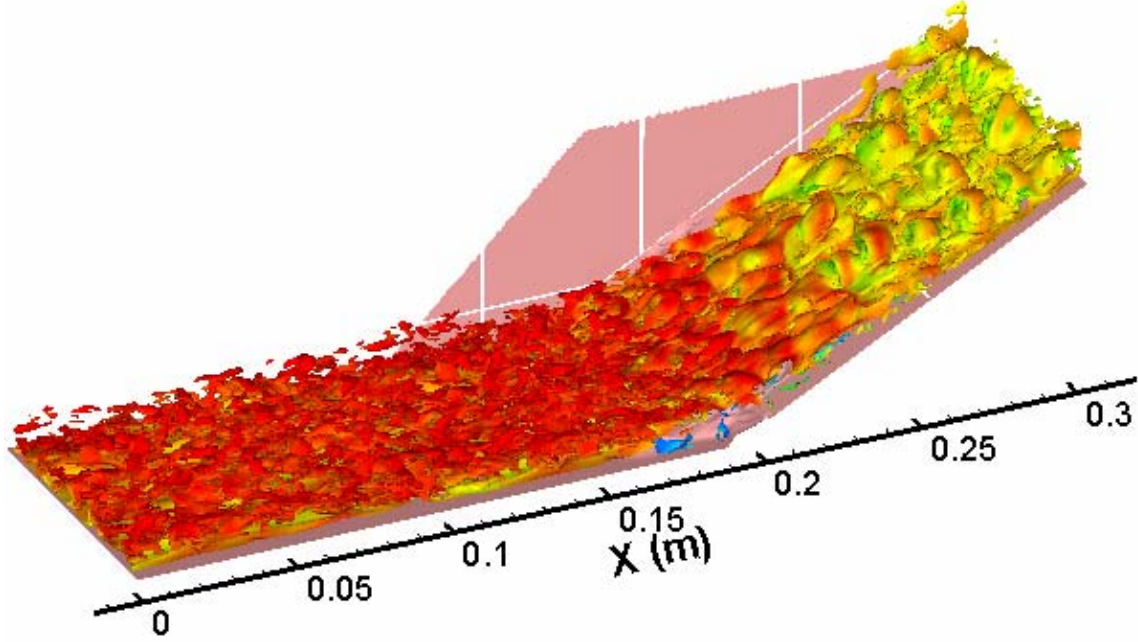


Figure 1: Isosurfaces of vorticity magnitude colored by axial velocity

$$T'_{\text{recyc}}|_{\text{lim}} = F_{\text{kleb}} T'_{\text{recyc}} \min(1.0, \left| \frac{T'_{\text{mork}}}{F_{\text{kleb}} T'_{\text{recyc}}} \right|), \quad F_{\text{kleb}} T'_{\text{recyc}} \neq 0 \quad (20)$$

The density fluctuation is determined as follows. First, a provisional value of the pressure fluctuation is determined from the recycled density fluctuation:

$$p'_{\text{prov}} = R[\rho_{\text{RANS}} T'_{\text{recyc}}|_{\text{lim}} + F_{\text{kleb}} \rho'_{\text{recyc}} (T_{\text{RANS}} + T'_{\text{recyc}}|_{\text{lim}})] \quad (21)$$

The pressure fluctuation is then limited to be a specified multiple of the pressure (2% in this case):

$$p'_{\text{prov}}|_{\text{lim}} = \text{sgn}(p'_{\text{prov}}) \min(|p'_{\text{prov}}|, 0.02 p_{\text{RANS}}) \quad (22)$$

and a corrected value of the density fluctuation is determined from the limited pressure fluctuation:

$$\rho'_{\text{recyc}} = (p'_{\text{prov}}|_{\text{lim}} - \rho_{\text{RANS}} R T'_{\text{recyc}}|_{\text{lim}}) / (T_{\text{RANS}} + T'_{\text{recyc}}|_{\text{lim}}) \quad (23)$$

4. Calculation Details

4.1. Test Geometry and Boundary Conditions

The test geometry is a 28 degree compression ramp placed on the floor of the University of Texas Mach 5 blowdown wind tunnel.[5] Several specific ramp configurations, differing primarily in the width of the ramp, have been used. The one modeled in this investigation (Ramp 3 in [5]) is 3.5 inches wide. Aerodynamic fences are attached to both sides of the ramp. The precise dimensions of the fences are not given in [5], though it is stated that the leading edge

of the fence at the tunnel wall extends 2.75 inches upstream of the ramp leading edge. Figure 1 shows isosurfaces of vorticity magnitude (50000 s^{-1}), colored by axial velocity. The position of one of the fences is indicated. The effects of the fences are included in the three-dimensional calculations by imposing solid wall boundary conditions over the portions of the Z_{\min} and Z_{\max} grid planes that are within the fence area. Otherwise, periodic boundary conditions are imposed at these planes. The mesh spacing in the spanwise (Z) direction is uniform, thus boundary layer growth on the fences is not resolved. The tunnel / ramp surface (Y_{\min}) is treated as an adiabatic wall. An extrapolation condition is used at the upper boundary (Y_{\max}) and at the outflow boundary (X_{\max}). The recycling /rescaling technique mentioned above is used to provide a time-dependent inflow boundary condition at X_{\min} . The computational domain extends from $X_{\min} = 0 \text{ m}$ to $X_{\max} = 0.304 \text{ m}$ in the streamwise direction, from $Z_{\min} = -0.0444 \text{ m}$ to $Z_{\max} = 0.0444 \text{ m}$ in the spanwise direction, and from $Y_{\min} = 0 \text{ m}$ to $Y_{\max} = 0.0635 \text{ m}$ (relative to the plate surface) in the vertical direction. The ramp leading edge is located at $X = 0.1905 \text{ m}$. The baseline mesh contains 360 cells in the X direction, 144 cells in the Y direction, and 129 cells in the Z direction (6.687 million cells in total). The mesh is clustered to the plate surface using a hyperbolic tangent stretching function so that the minimum d_w^+ in the inflow boundary layer is around one. The mesh spacing is uniform in the X and Z directions and is chosen such that approximately 20 cells would be located within one boundary layer thickness (0.0175 m). One simulation was performed on a mesh with smaller spacing (60% of the baseline value) in the interaction region. This mesh contains 480 cells in the X direction, thus raising the total number of cells to 8.916 million. For the remainder of this paper, the X coordinate is redefined to represent the distance along the surface of the geometry. and the origin is located at the wedge apex. The Y coordinate is redefined to represent the coordinate normal to the surface.

4.2. Initialization Procedure and Time Evolution Details

The calculations were initialized by first computing a 2-D flat plate solution for the incoming boundary layer. A target inflow profile was determined as the location where the computed boundary layer properties best matched the experimental values shown in Table 1.

Table 1: Inflow boundary layer properties

Parameter	Value
M_{∞}	4.95
p_o (Pa)	2.17e6
T_o (K)	350
Re/m	50.1e6
δ_o (cm)	1.75
δ^* (cm)	0.63
θ (cm)	0.00513
C_f	7.83e-4

The test section in the experiments is just downstream of the wind-tunnel nozzle exit. Details of the nozzle geometry were not available, so the above procedure was used to provide a representative inflow. The inflow profile was extracted from the flat-plate data and used to

initialize a 2-D RANS calculation of the entire interaction. As discussed in Section 5.5, the choice of the constant A_{sst} has a pronounced effect on the prediction of the upstream extent of axial separation; the 2-D RANS data corresponding to $A_{sst}=0.9$ was used to initialize the three dimensional hybrid LES / RANS calculations.

To accelerate the development of coherent structures, a velocity fluctuation field obtained from a previous LES/RANS simulation of a Mach 3 boundary layer at a Reynolds number / meter of 49.5e6 [25] was superimposed upon the RANS base state upstream of the wedge apex. The Mach 3 velocity fluctuation field was expanded in the periodic Z (spanwise) and assumed periodic X (streamwise) directions to cover the X-Z extent of the flat-plate region. The velocity fluctuations from the Mach 3 simulation were scaled by the ratio of the friction velocities,

$$u'_i|_{M=5} = u'_i|_{M=3} \left(\frac{u_\tau|_{M=5}}{u_\tau|_{M=3}} \right) , \quad (24)$$

and all coordinates were scaled by the ratio of the boundary layer thicknesses,

$$x_i|_{M=5} = x_i|_{M=3} \left(\frac{\delta_0|_{M=5}}{\delta_0|_{M=3}} \right) \quad (25)$$

to provide a reasonable match with the Mach 5 flow. Equation (19) was then used to provide the temperature fluctuation field, and an assumption of negligible pressure fluctuations was used to provide the density fluctuation field. Wu, et al. [26] have reported the use of a similar initialization technique in their DNS calculations.

Starting from this initial condition, a hybrid LES/RANS solution with $A_{sst} = 0.9$ was evolved at a time step of 2e-7 s for 3.5 ms ($155 \delta_0 / u_\infty$) to eliminate initial transients. Complete time histories for several planes of data ($Z/\delta_0 = 0.0$, $Y/\delta_0 = 0.0$, $Y/\delta_0 = 0.2$, $Y/\delta_0 = 0.7$, $X/\delta_0 = -3.5$, $X/\delta_0 = 0.0$, $X/\delta_0 = 4.0$) were then collected for an additional 8 ms ($354 \delta_0 / u_\infty$). The sampling period was 2e-6 s. Flow-property data was also averaged in time and in space over the interval $-1.8 < Z/\delta_0 < 1.8$ to yield nominally two-dimensional statistics. The solution obtained after 11.5 ms was used as the initial condition for three additional runs: $A_{sst} = 0.0$, $A_{sst} = 0.9$ on the refined mesh, and $A_{sst} = 1.0$. In these cases, the solutions were evolved for 3.0 ms without gathering statistics. Statistics were then collected for a minimum of 8 ms beyond this point.

5. Results and Discussion

5.1. Flat Plate Boundary Layer

Axial velocity profiles in wall coordinates are compared with experimental data [5] in Figure 2. These profiles, as well as those shown in Figure 3, were extracted at the recycle-plane location ($\sim 7 \delta_0$ downstream of the inflow plane). The RANS and hybrid LES/RANS solutions slightly over-predict the experimental data but are virtually indistinguishable from one another. The time-averaged position of the blending function is also indicated. The $\Gamma=0.9$ position is at $d_w^+ = 266.1$, while the $\Gamma=0.5$ position is at $d_w^+ = 344.5$. The target d_w^+ location, defined according

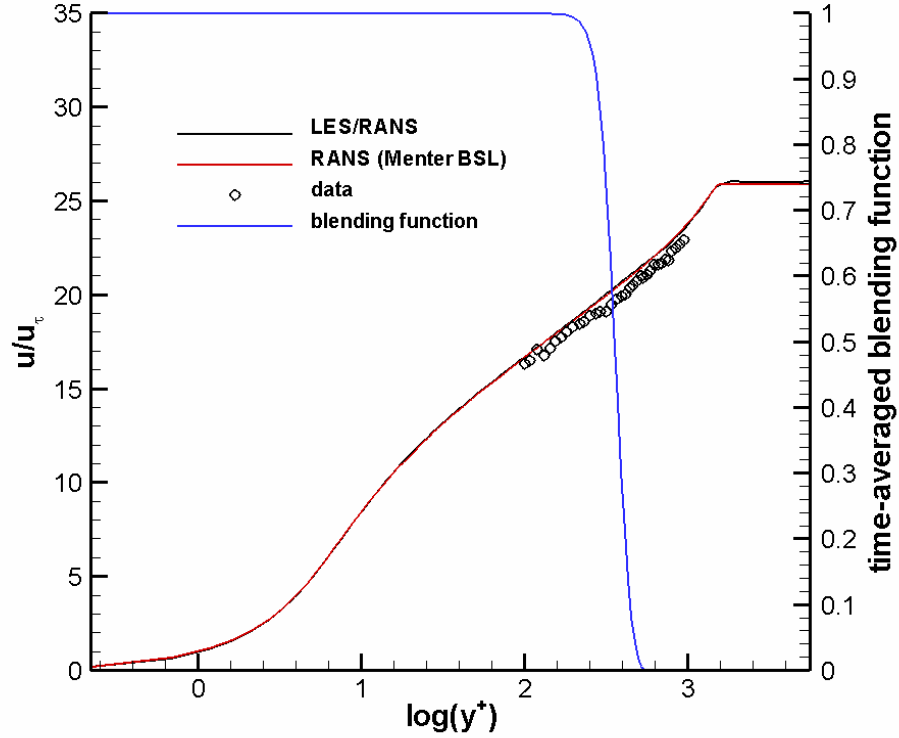


Figure 2: Inflow boundary layer velocity profile and blending function position (wall coordinates)

to the criteria outlined in Section 3.2, is 345.5, so it is clear that the predicted average position of the blending function is obtained in the simulations.

Figure 3 compares Reynolds stress components and *rms* mass flux fluctuation data with experimental data from Smits and Muck [27] at Mach 2.79, $Re/m = 63.0e6$, as comparable Reynolds stress data for the actual Mach 5 experiments could not be located. The Reynolds stress components are scaled by $\rho_w u_\tau^2$ while the *rms* mass flux fluctuation is scaled by $\rho_\infty u_\infty$, thus providing a measure of the turbulence intensity. Agreement with experimental data for the normal stress component $\langle \rho u'' u'' \rangle$ is good, but the predictions for the resolved shear stress component $\langle \rho u'' v'' \rangle$ show a larger constant-stress region (extending to approximately $Y/\delta_{loc} = 0.4$) that is indicated in the experimental data. This leads to an over-prediction of the Reynolds shear stress in the outer part of the boundary layer. The sum of the modeled $\langle \rho u'' v'' \rangle$ component (also shown) and the resolved $\langle \rho u'' v'' \rangle$ component extends the constant-stress region further toward the wall, and the maximum normalized shear stress is around one, as expected from inner-layer scaling theory. The prediction for the normal stress component $\langle \rho v'' v'' \rangle$ also displays a maximum value at $Y/\delta_{loc} \sim 0.4$, which is outside the logarithmic layer. This unexpected behavior seems to be related to the response of the recycling / rescaling method as applied to wall-normal velocity component and is the subject of current study. The mass flux fluctuation profile agrees reasonably well with the experimental data

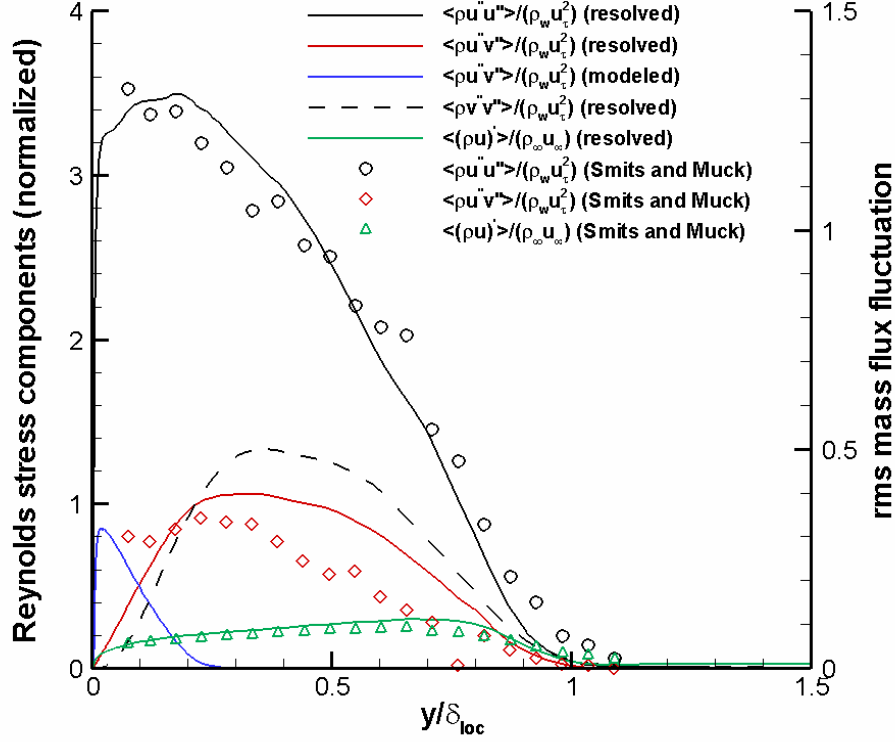


Figure 3: Reynolds stress and mass-flux fluctuation profiles in inflow boundary layer

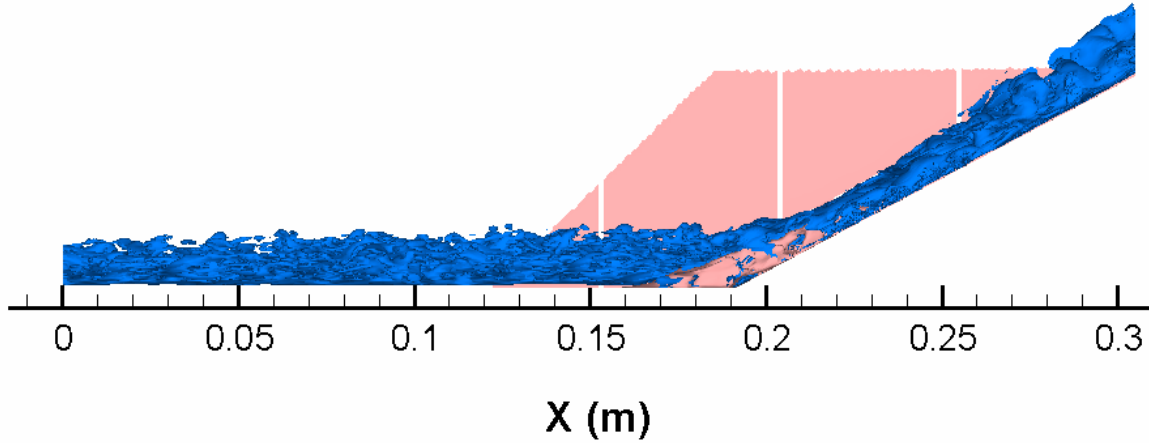


Figure 4: Isosurfaces of axial vorticity (side view)

though the peak value is slightly over-predicted. Except for the Reynolds shear stress response in the outer layer (which could lead to faster boundary layer growth that anticipated), the equilibrium boundary layer structure appears to be well-predicted by the hybrid LES/RANS model.

5.2. Three-Dimensional Flow Structure

Some aspects of the instantaneous flow structure are illustrated in Figures 1, 4 and 5. Vorticity iso-surfaces in Figures 1 and 4 reveal an increase in the length scale and an increase in the

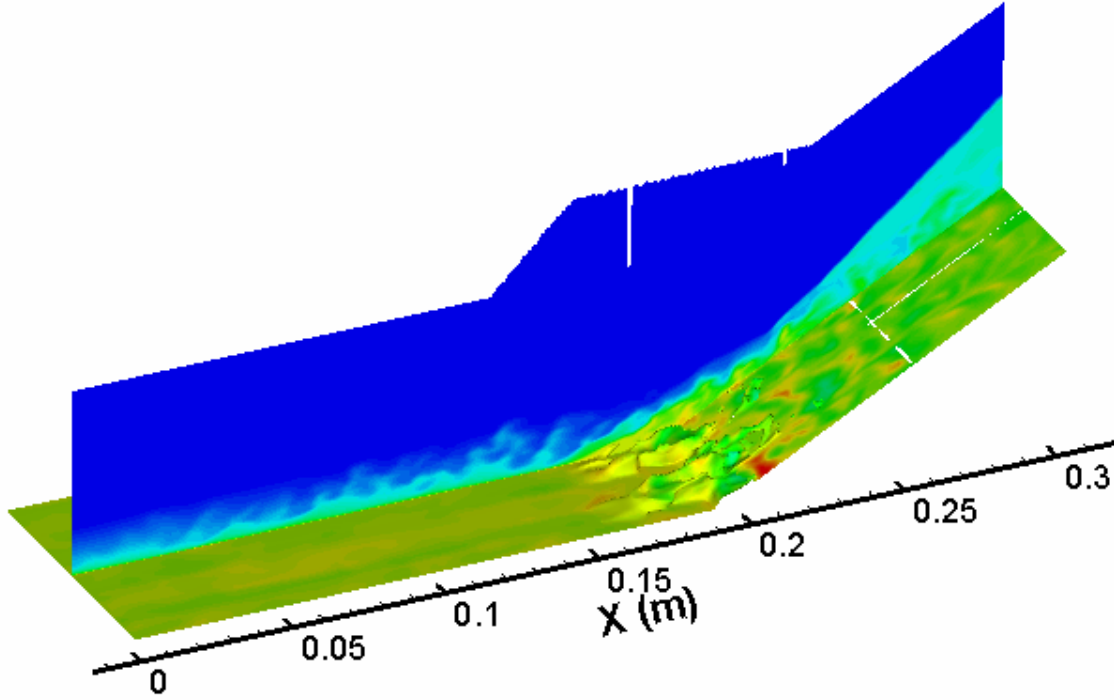


Figure 5: Isosurfaces of zero axial velocity colored by temperature

coherence of the turbulent structures as they move through the shock system. Smaller-scale structures seem to be attenuated as the flat plate boundary layer shifts to a wake-like pattern upon detaching from the surface, and upon re-attaching on the ramp, larger vortical structures are formed. Figure 5 shows an isosurface of zero axial velocity colored by the mean temperature. The regions of separated flow are not continuous across the span of the domain and they taper to a point when re-attaching on the ramp surface. High wall temperatures are found in the vicinity of the reattachment locations.

Time-averaged predictions of wall skin friction are shown in Figure 6, and corresponding line plots are shown in Figure 7. Results from three different simulations, $A_{sst} = 0.0$, $A_{sst} = 0.9$, and $A_{sst} = 1.0$, are illustrated in Figure 6. The incoming boundary layer and the region of reversed flow (darker blue) are nominally two dimensional. Some small peaks and valleys in the skin friction distributions are evident upstream of the wedge apex, but the positions are different among the simulations. This indicates that, with sufficient time evolution, a statistically two-dimensional flow would probably be obtained upstream of the wedge apex. The situation is different in the re-attachment / recovery region. Here, the peaks and valleys in the distributions are much more prominent, with the regions of lower skin friction corresponding to the extension of pockets of low-momentum fluid further onto the ramp surface. In their LES simulation of Mach 3 flow over a compression corner, Loginov, et al. [14] also observe this topology and attribute it to the presence of pairs of counter-rotating streamwise vortices in the re-attaching shear layer. Experimental oil-flow images presented in [28] also show evidence of these structures. The regions of lower skin friction (green in the figure) correspond to the action of the vortices in lifting fluid away from the wall, while the regions of higher skin friction (red) correspond to the vortices' forcing higher-momentum fluid toward the wall. In the present

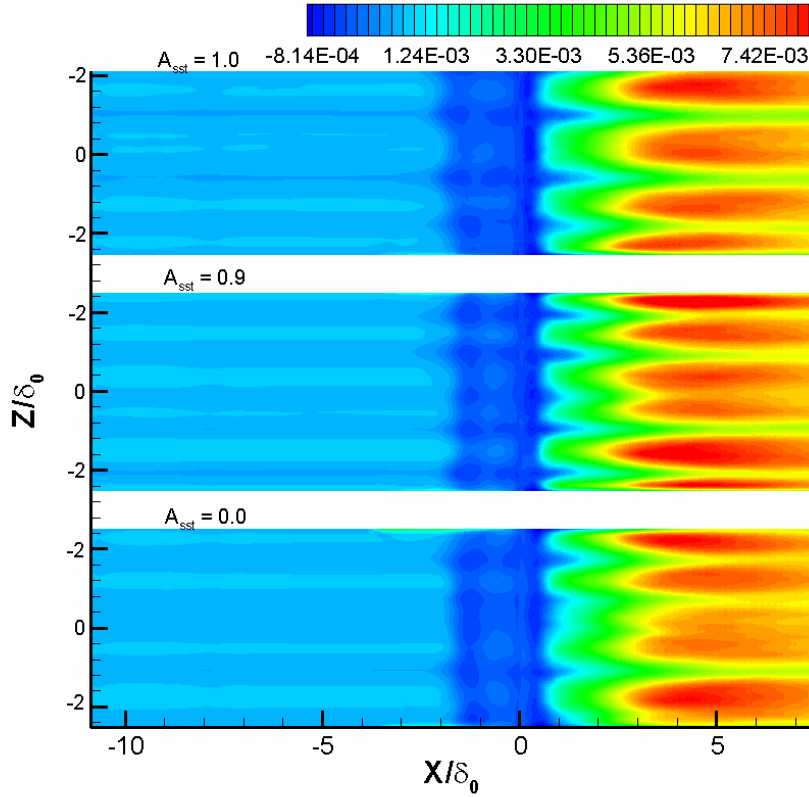


Figure 6: Contours of time-averaged wall skin friction

simulations, the spanwise positioning of the structures correlates with weaker spanwise inhomogeneities in the incoming boundary layer; the same effect is seen in the simulations of Loginov, et al. [14]. The distance between lines of convergence (green contours) provides a measure of the size of the dominant vortex pairs. We find that these sizes range from $\sim 1.2 \delta_0$ to $2.0 \delta_0$, which may be compared with a value of $\sim 2.0 \delta_0$ in Loginov, et al.'s calculations. Loginov, et al. also argue that the growth of these structures may result from a Görtler instability mechanism, given the degree of streamline curvature present as the boundary layer separates, then re-attaches on the wedge surface. Navarro-Martinez and Tutty [29] have observed the formation and evolution of Görtler-type vortices in simulations of hypersonic laminar flow over a compression ramp. The size of the vortex pairs in their work is approximately the same as the incoming boundary layer thickness. As the vortical structures appear to originate from amplification of inhomogeneities present in the inflow boundary layer, the time-averaged positions of the vortices on the ramp surface are likely to depend on the methods used to initiate and sustain the boundary layer and possibly on the total time elapsed during the simulation.

Figure 7 presents line plots of time-averaged skin friction at different spanwise positions for the $A_{sst} = 0.0$ LES/RANS case. Also shown is the span-averaged value and the result from a RANS calculation with $A_{sst} = 0.87$. As shown later, this choice for A_{sst} provides the best match with the upstream position of the separation shock as predicted by the LES/RANS method. The degree of spanwise variation about the mean value is noteworthy (-18% to +26% at the peak location),

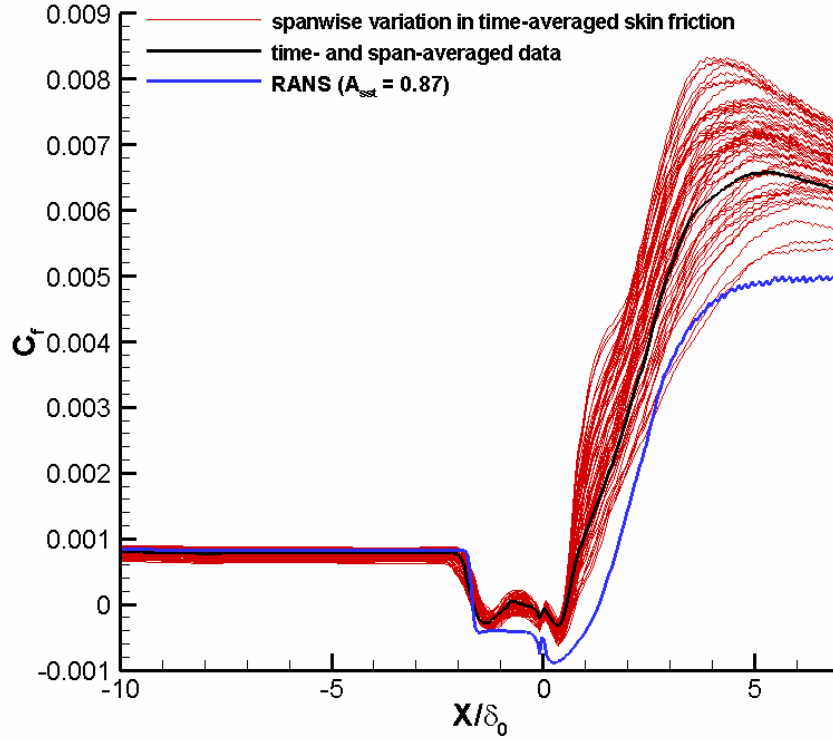


Figure 7: Spanwise variation of time-averaged skin friction

and at all stations, the skin friction values in the recovery region exceed those predicted by the RANS model. The high-frequency noise in the skin-friction distributions on the wedge surface is an artifact of a numerical precision problem in the data-reduction code and is not a feature of the computed flow field. Other comparisons with the RANS models are described in Section 5.5.

The presence of a range of frequencies in the unsteady motion of shock wave as it interacts with a boundary layer is well-documented in experiments. ([1] and references cited within). Turbulent eddies directly interact with the shock wave, producing ripples in the shock front that change their amplitude and positions over time scales representative of the motion of the individual eddies. Less well understood is the presence of a large-scale, low frequency oscillation of the entire shock system and the associated region of separated flow. [1] Recent wide-field planar light-scattering (PLS) measurements [8] suggest that this behavior may be associated with the sustained presence of elongated streaks of uniform-momentum fluid in the incoming boundary layers. These streaks have been shown to extend upwards of $30 \delta_0$ in a Mach 2 flow. In regions where the streaks have lower momentum than the average, the separation shock can move further upstream; the converse is true in regions where the streaks have higher momentum than the average. It is argued that the persistence of these streaks allows a low-frequency motion to develop, while individual-eddy interactions continue to provide a high-frequency component. In the LES/RANS simulations, we cannot calculate the entire evolution of the boundary layer in the wind tunnel. Furthermore, the use of recycling / rescaling would appear to force a length scale equal to the distance between the inflow plane and the

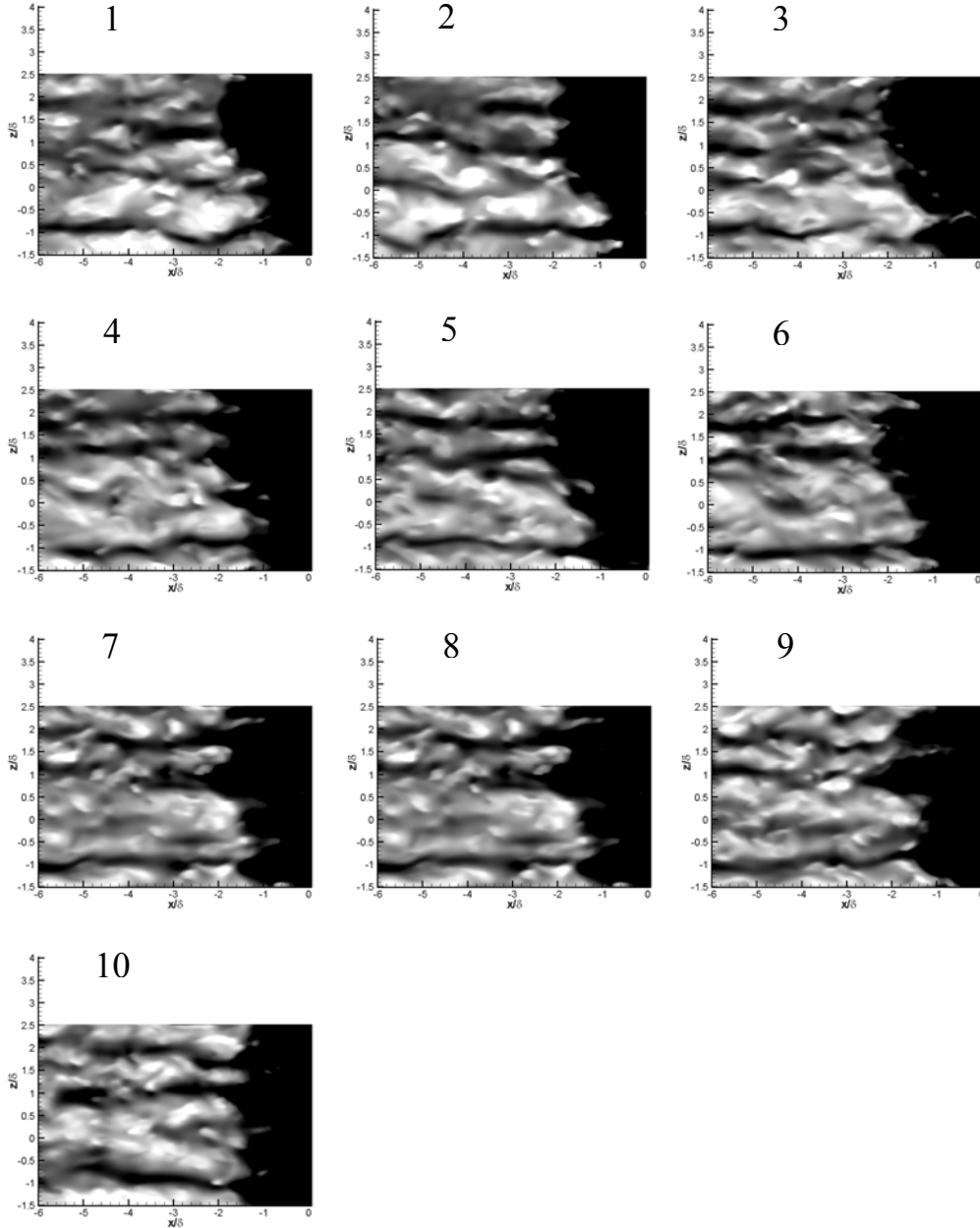


Figure 8: Snapshots of axial velocity at $Y/\delta_0=0.2$ (0.0001 s time intervals)

recycling plane ($7\delta_0$) onto the computed flow. As shown later, the frequency associated with this length scale is a noticeable part of the spectrum but is not a dominant part, and the technique can capture lower frequencies as well as higher ones. Figure 8 presents snapshots of the axial velocity within a plane located at $Y/\delta_0 = 0.2$. This location corresponds to that chosen for wide-field PLS imaging in [8]. The snapshots are numbered 1-10 with each successive snapshot separated by 0.0001 s. Contour levels are chosen to highlight regions of lower velocity (dark) and higher velocity (light) in the incoming boundary layer. The separation line is delineated as

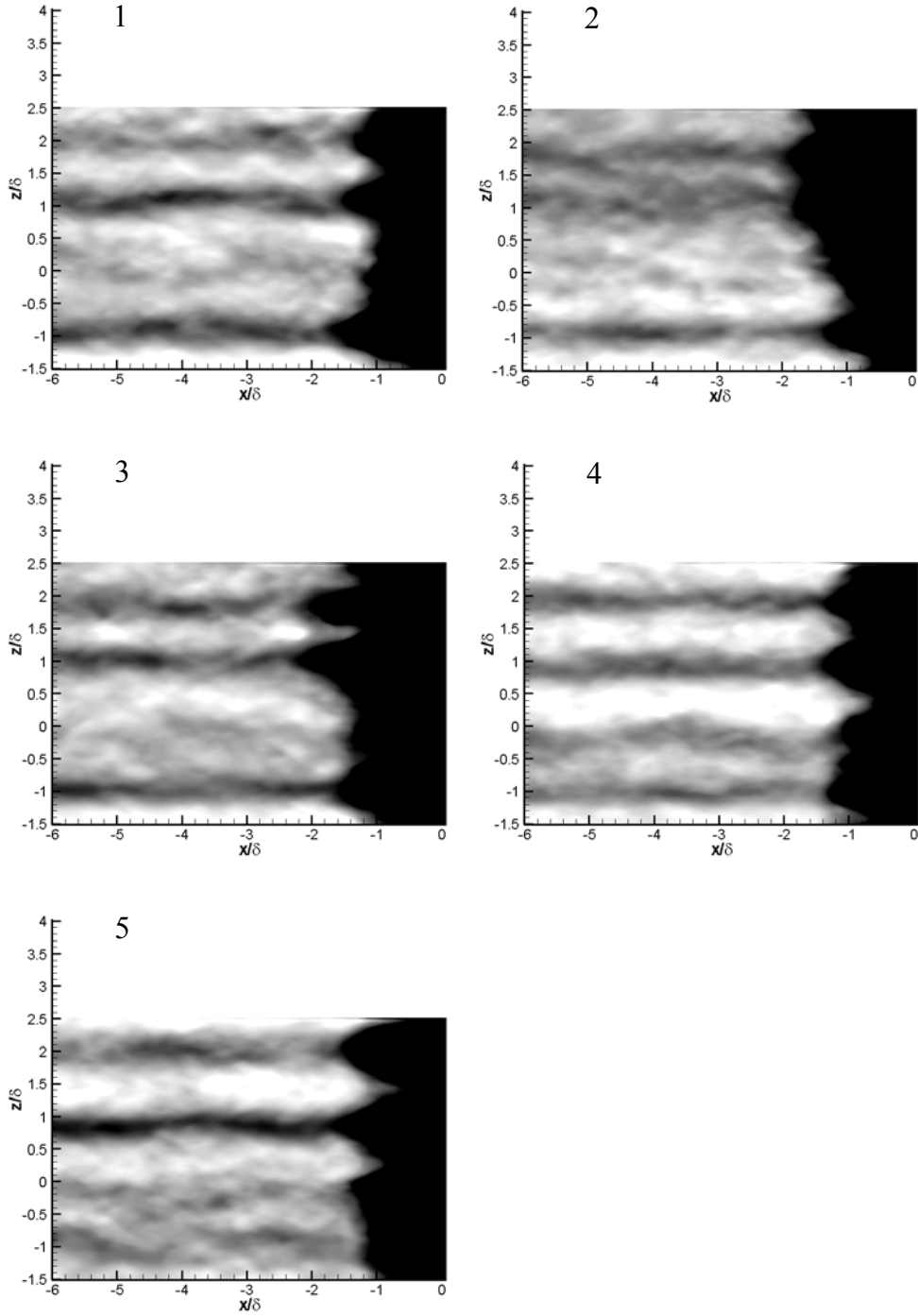


Figure 9: Snapshots of axial velocity at $Y/\delta_0=0.2$ (averaged over 0.001 s)

the onset of the dark black region at the left of the figures. There is clear evidence of a streak-like pattern in the incoming boundary layer. Frames 1-6 in the snapshot sequence (extracted from the $A_{sst} = 0.9$ simulation on the baseline mesh) show that the separation region is located

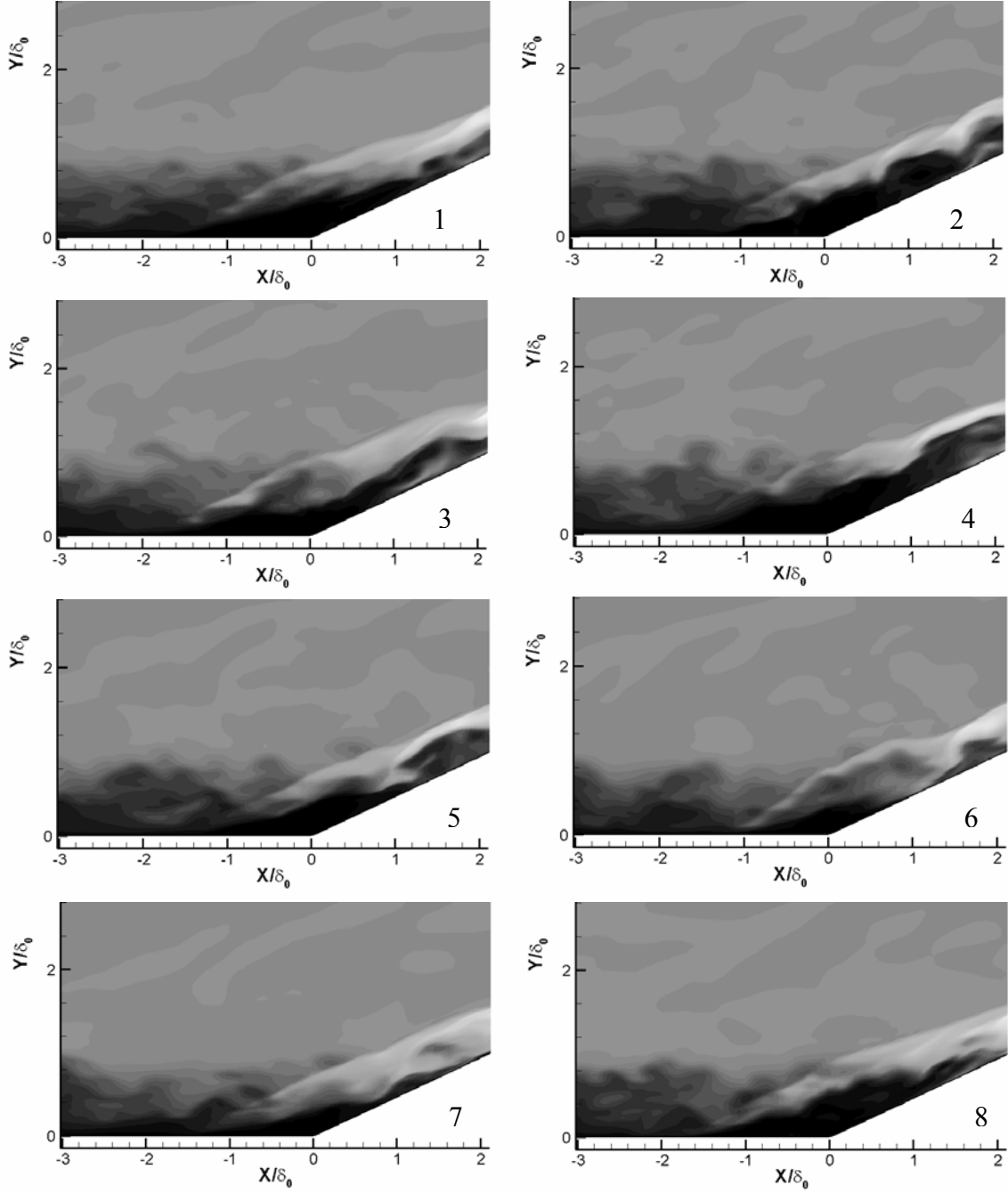


Figure 10: Snapshots of vertical velocity in X-Y centerplane (0.001 s time intervals)

further upstream toward the upper side fence (top) and that this upstream positioning is correlated with a general darkening of the contours, indicating the sustained presence of lower-momentum fluid. At later times, higher-momentum streaks of fluid eventually enter this region and act to push the separation line further downstream. The separation line position near the lower side plane does not migrate as much over this time interval. The passage of individual streaks of fluid into the separation zone results in local perturbations to the separation line, but it is the collective effect of several neighboring streaks with approximately uniform momentum

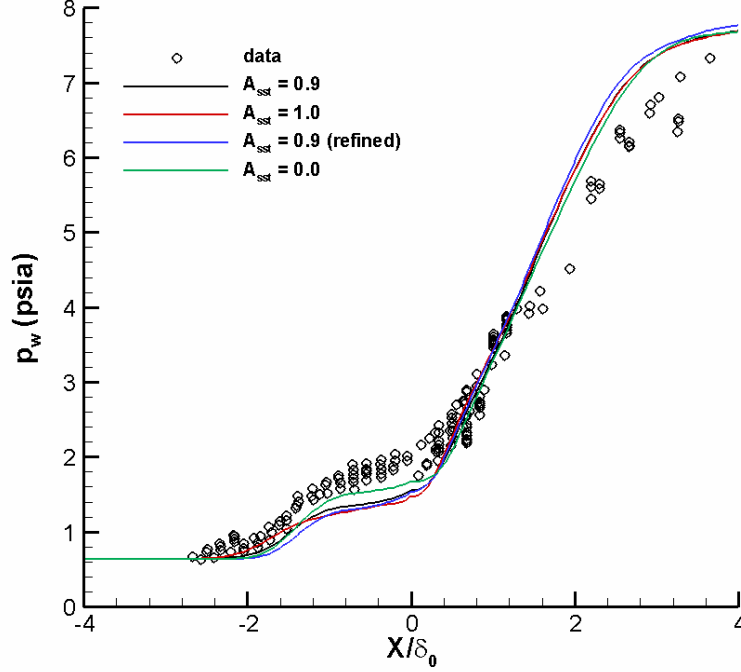


Figure 11: Wall pressure distributions (LES/RANS models)

that appears to induce the larger-scale dynamics. Animations reveal this process in more detail and are included as supplements to this report. Figure 9 presents snapshots of the velocity field averaged over successive periods of 0.001 s. Frame 2 in this sequence corresponds to the event illustrated in detail in Figure 8. Frames 1, 3, and 4 indicate the effects of isolated streaks of low / high momentum fluid in locally modulating the separation line, and the collective effect of a group of higher-momentum streaks in pushing the separation line further downstream is shown at the bottom of Frame 5.

Figure 10 presents snapshots of vertical (v) velocity contours in the interaction region, extracted every 0.001s along the $Z/\delta_0 = 0.0$ centerplane from the $A_{sst} = 0.0$ simulation data. The view corresponds approximately to that imaged by Noel Clemens' group at the University of Texas [30] using time-resolved PLS techniques. The snapshots show a highly dynamic motion of the separation shock. Its progression forward (Frames 4, 6, and 8) appears to be accompanied by the thickening of the separation region (indicated in dark contours) while its travel upstream (Frames 1 and 3) is associated with the elongation and thinning of the separation region. The boundary layer changes dramatically as the fluid moves through the separation shock and re-attaches on the ramp surface. Larger, more two-dimensional eddies form in the wake-like region above the separation zone, and their passage downstream deforms the re-attachment shock plane significantly. The animations included in this report provide more details of this process.

5.3. Comparisons with Experimental Mean Flow Data

Mean flowfield data obtained in the Dolling-group experiments includes average wall pressure distributions (some conditioned on the separation shock position), pressure fluctuation variance

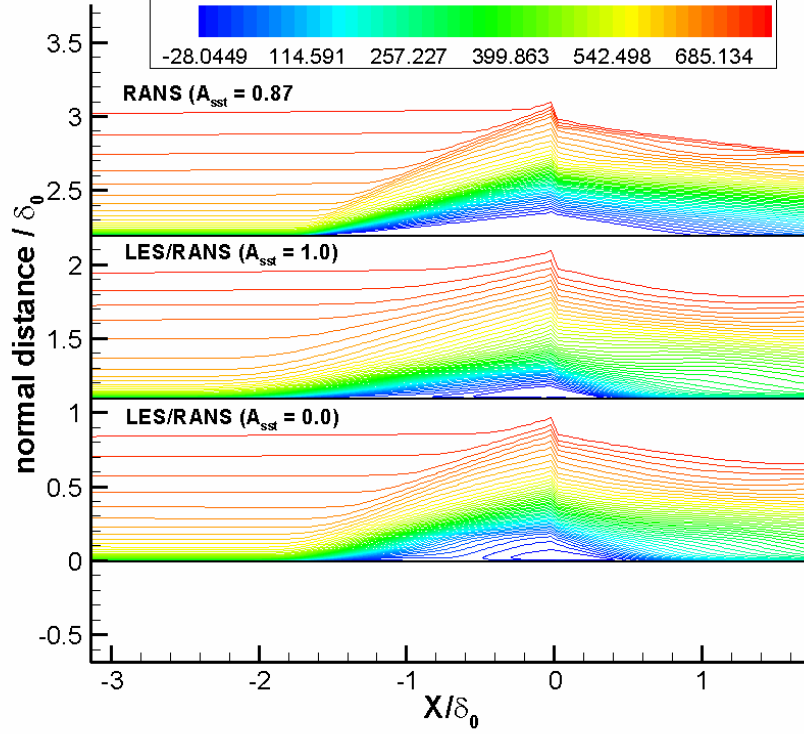


Figure 12: Time- and span-averaged axial velocity contours in the interaction region

distributions, and pitot pressure distributions in the re-attachment region. Most of these measurements were taken along the centerline of the configuration. To generate smoother statistics and thereby approximate a longer time sequence than is actually available in the simulations, we have elected to average most of data over the interval $-1.8 < Z/\delta_0 < 1.8$ in the spanwise direction. This eliminates regions of the flow that are nearest to the fences from directly affecting the time averages. Wall pressure distributions are shown in Figure 11 for each of the LES/RANS simulations. Several trends are apparent. While the general shape of the pressure distribution upstream of the wedge is predicted accurately, all of the calculations under-predict the pressure level in this region. Since the separation-shock pressure rise is a result of the displacement effect of the separation bubble, this trend indicates that no approach correctly predicts the vertical extent of the separation region. The separation-shock pressure rise appears to take place gradually over a distance of about 1 to 1.5 δ_0 . This response is a result of the averaging effects of the separation shock motion, and all predictions capture this feature to good accord. The $A_{sst} = 0.0$ calculation provides the best overall agreement with the experimental data in the separation region, even though the upstream extent of the separation bubble is slightly under-predicted. The $A_{sst} = 1.0$ calculation results in an elongated separation bubble that provides only a small displacement effect. The $A_{sst} = 0.9$ calculations performed on the baseline and refined meshes provide generally similar results, but it is clear that localized mesh refinement does not improve agreement with experimental data. The pressure level on the wedge surface is in excess of that measured in the experiments. This is a consequence of the under-prediction of the size of the separation region and the separation-shock strength. Other differences between the model predictions are noted in Figure 12, a plot of time-averaged axial velocity contours in the interaction region. The vertical axis is the normal distance from the surface. As such, there

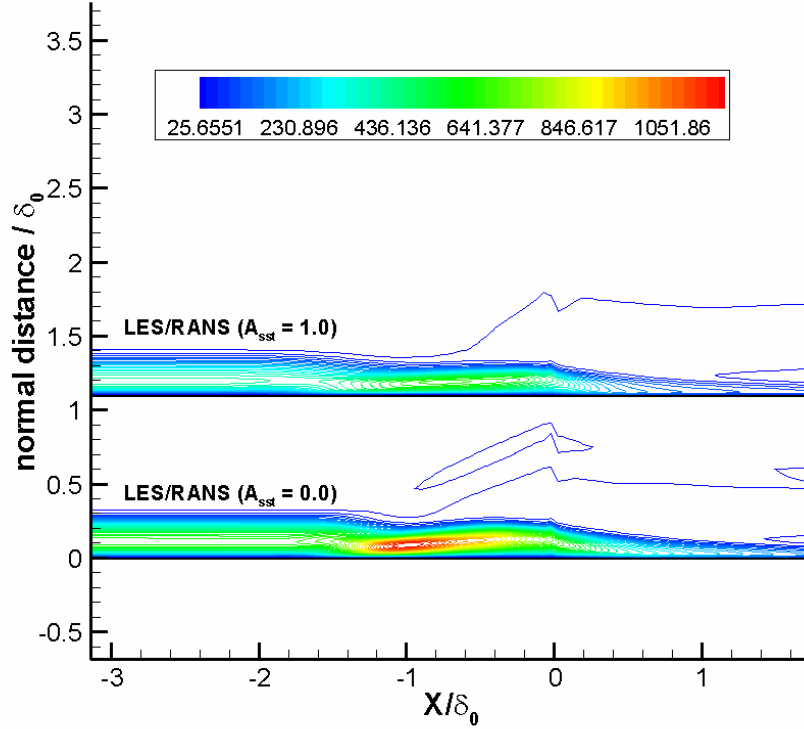


Figure 13: Time- and span-averaged kinematic eddy viscosity contours in the interaction region

is a discontinuity at the wedge apex, and all data is interpolated onto normal lines extending away from the surface. Also shown in the comparison is a prediction from the baseline RANS model with $A_{sst}=0.87$. The enhanced vertical displacement of the separation bubble in the $A_{sst}=0.0$ LES/RANS calculation, relative to that of the $A_{sst}=1.0$ calculation, is clearly indicated. The bubble size and shape in the $A_{sst}=0.0$ LES/RANS calculation is comparable to that predicted by the RANS model, but the velocity field within the bubble itself is clearly different. Kinematic eddy viscosity profiles (normalized with respect to the free-stream kinematic viscosity) shown in Figure 13 for the $A_{sst}=0.0$ and $A_{sst}=1.0$ LES/RANS models indicate the expected result of a lower eddy viscosity when the SST modification is fully active. This appears to lower the resistance of the near-wall flow to the adverse pressure gradient, allowing more upstream propagation to take place but in turn, reducing the thickness of the separation bubble. It is clear from the contours that this reduction in bubble displacement weakens the separation shock.

Predictions of the standard deviation of the wall pressure fluctuations are presented in Figure 14. The general shape of the experimental distribution is captured, but the peak in fluctuation intensity near the separation shock is under-predicted by all models. The $A_{sst}=0.9$ calculation on the baseline mesh best predicts the position of the peak. It should be noted that the magnitude of the peak (but not its location) is well-predicted by the $A_{sst}=0.0$ calculation if the data is sampled at $Y/\delta_0=0.2$ instead of at the wall. This result may imply that the enhanced eddy viscosity provided by RANS model in the near-wall region damps the separation-shock motion to some degree. All calculations capture the fluctuation intensity level in the pressure plateau region

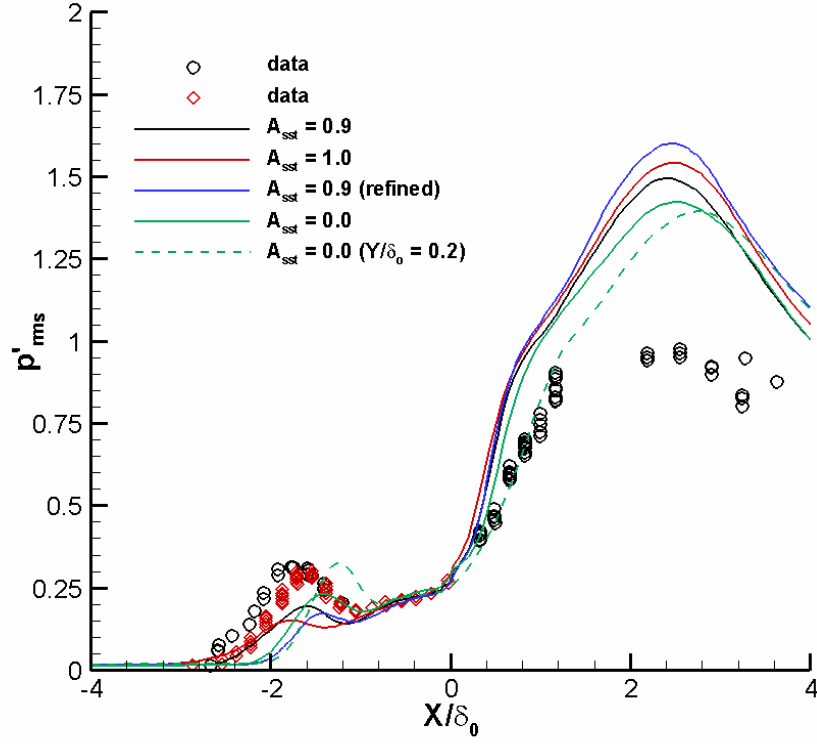


Figure 14: *rms* pressure fluctuation distributions (hybrid LES/RANS models)

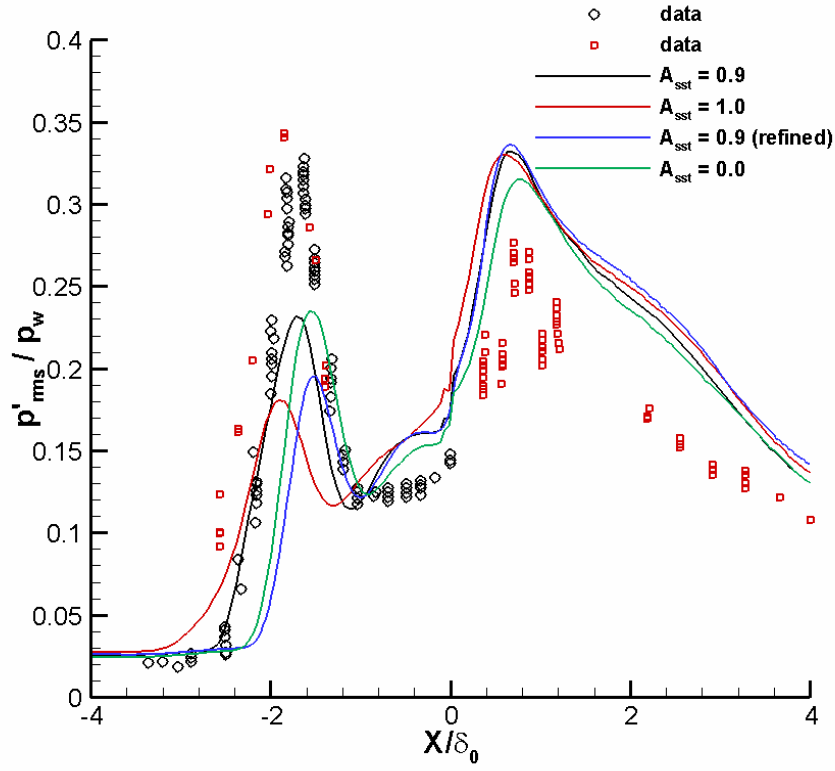


Figure 15: *rms* pressure fluctuation distributions normalized by local wall pressure

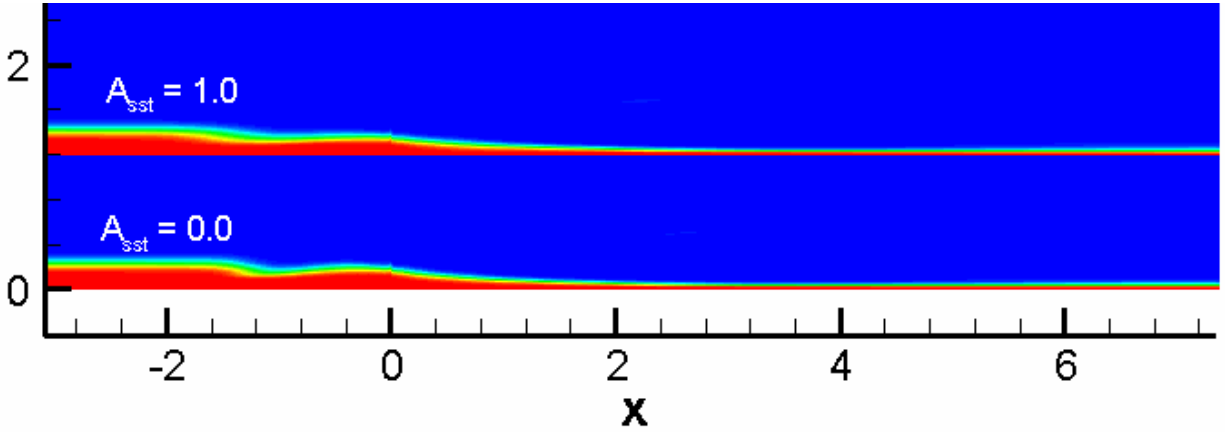


Figure 16: Time- and span-averaged blending function in the interaction region (vertical coordinate is normal to the surface)

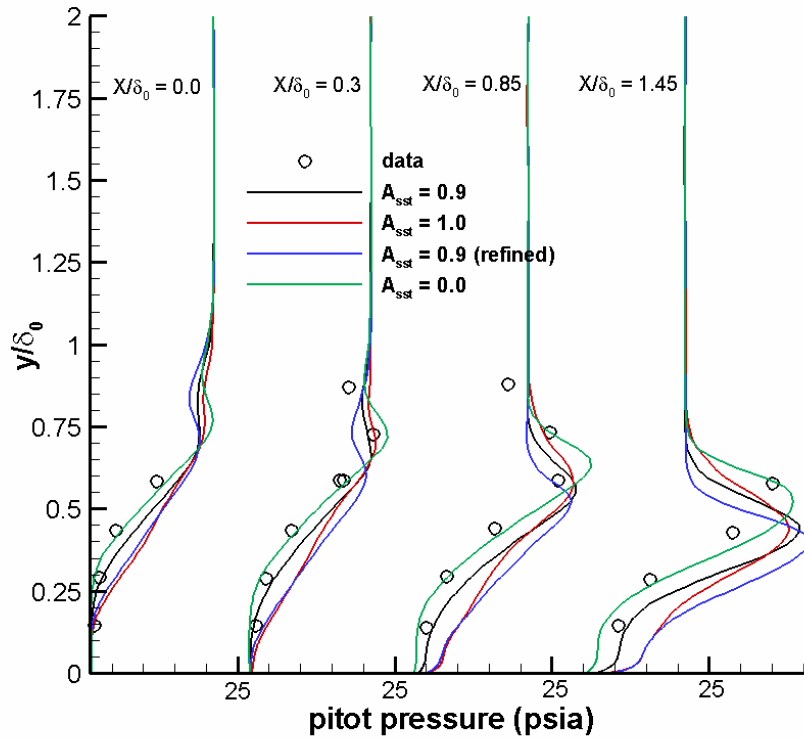


Figure 17: Pitot pressure profiles in re-attachment region

upstream of the corner, but all over-predict the intensity level in the re-attachment and recovery regions. As the wall pressure itself is also over-predicted in this region, it is useful to examine the *rms* values normalized by the local wall pressure. Figure 15 shows that none of the calculations correctly capture the relative distributions of fluctuation intensity due to separation-shock motion and due to shear layer re-attachment and re-attachment shock motion. Whereas the under-prediction of the peak in fluctuation intensity near the separation shock may be due to

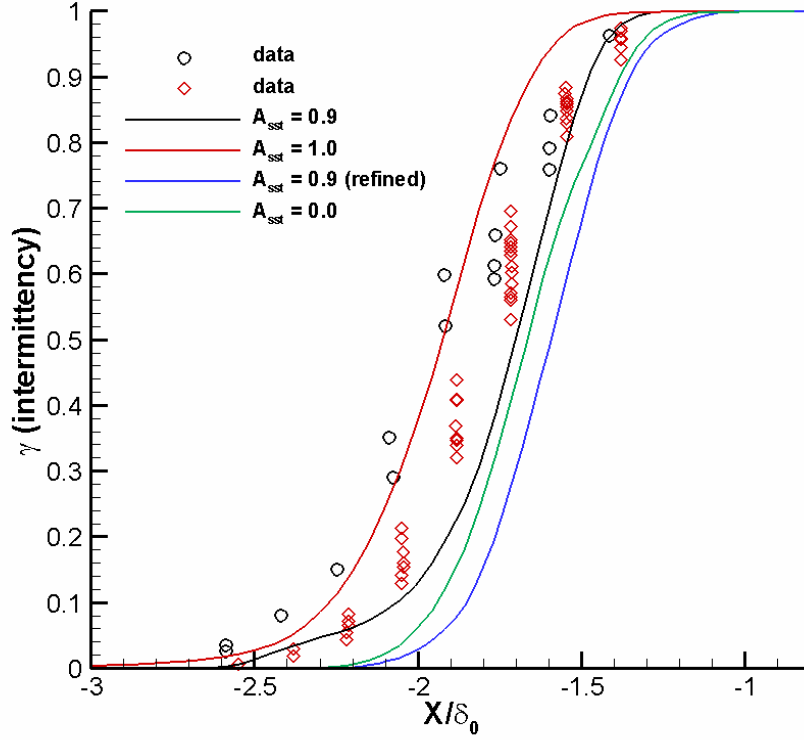


Figure 18: Separation-shock intermittency distributions

the damping effect of the near-wall RANS model, the opposite may be true on the ramp surface. Figure 16 plots the time- and span-averaged blending function in the interaction region. Downstream of re-attachment, the blending function collapses toward the wall, meaning that more of the recovering boundary layer is modeled as a large-eddy simulation. The near-wall resolution may be insufficient to capture the proper decay of turbulence energy, and the fluctuation intensity level at the surface may be over-predicted as a result. The collapse in the blending function is a direct result of an increase in the turbulence frequency ω as the flow passes through the shock system. Efforts are underway to understand this behavior better and to develop modifications that may control the response. Even with this effect, it is likely that further improvements in the prediction of the separation-shock strength and the upstream extent of the separation zone would result in better predictions of the fluctuation intensity throughout the interaction.

Predictions of pitot pressure at several stations just downstream of the corner are compared with experimental data from [4] in Figure 17. The best result is provided by the $A_{sst} = 0.0$ calculation, which captures the wake-like structure of the re-attaching boundary layer correctly at all positions. For the other models, the peaks in the pitot pressure distribution are positioned closer to the wall and the boundary layer appears to accelerate more rapidly than is indicated in the experimental data.

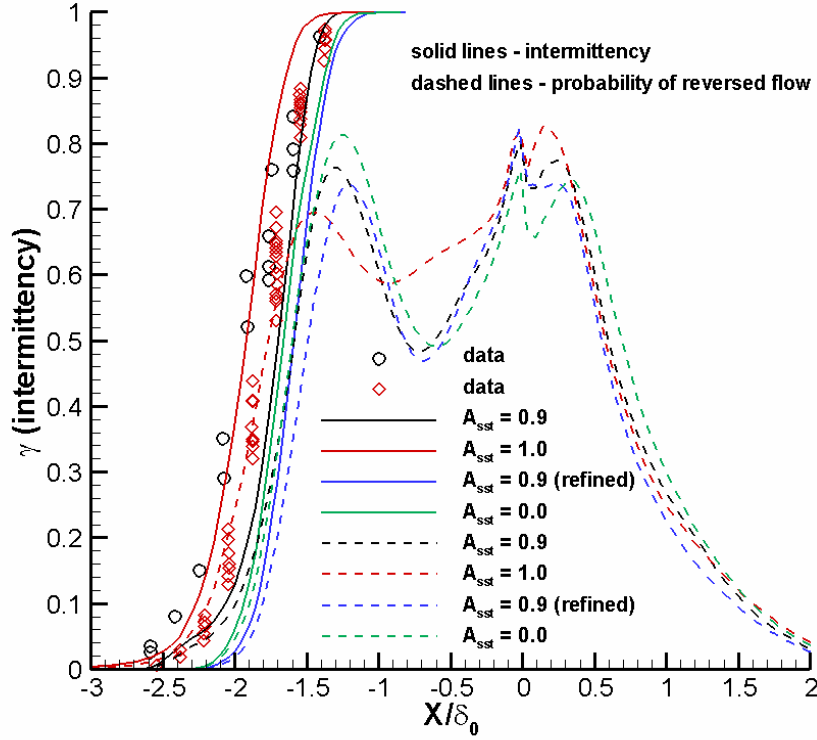


Figure 19: Separation-shock intermittency and probability of reversed flow

5.4. Dynamics of Shock-System Motion

References [5] and [6] describe the use of conditional sampling techniques to examine the motion of the shock-induced separation region and the resulting effects on the wall pressure profiles. We have performed similar analyses using the wall pressure data extracted in the LES/RANS simulations. Again, spatial homogeneity is assumed over the $-1.8 < Z/\delta_0 < 1.8$ interval in order to increase the sample size. Figure 18 shows the intermittency of the separation-shock position. At a particular X station, the intermittency (γ) is defined as the fraction of time that the separation shock is ahead of this position. A value slightly greater than zero corresponds to the most upstream positioning of the separation shock, while a value slightly less than one corresponds to the most downstream positioning of the separation shock. The most probable position of the separation shock is indicated by an intermittency value of 0.5. The general shape of the experimental intermittency distribution is captured by all LES/RANS models, though the extent of the separation-shock motion appears to be slightly under-predicted. The most probable position of the separation shock in the experiment is around $-1.8 X/\delta_0$; the $A_{sst} = 1.0$ prediction ($-1.95 X/\delta_0$) and the $A_{sst} = 0.9$ prediction on the baseline mesh ($-1.7 X/\delta_0$) bracket the experimental result. Figure 19 plots the separation-shock intermittency distribution along with a measure of the probability of having reversed axial flow near the surface. A value of one at a given location means that for the entire sample time, the axial velocity is negative. As shown, there is no station that maintains reversed flow at all times, and

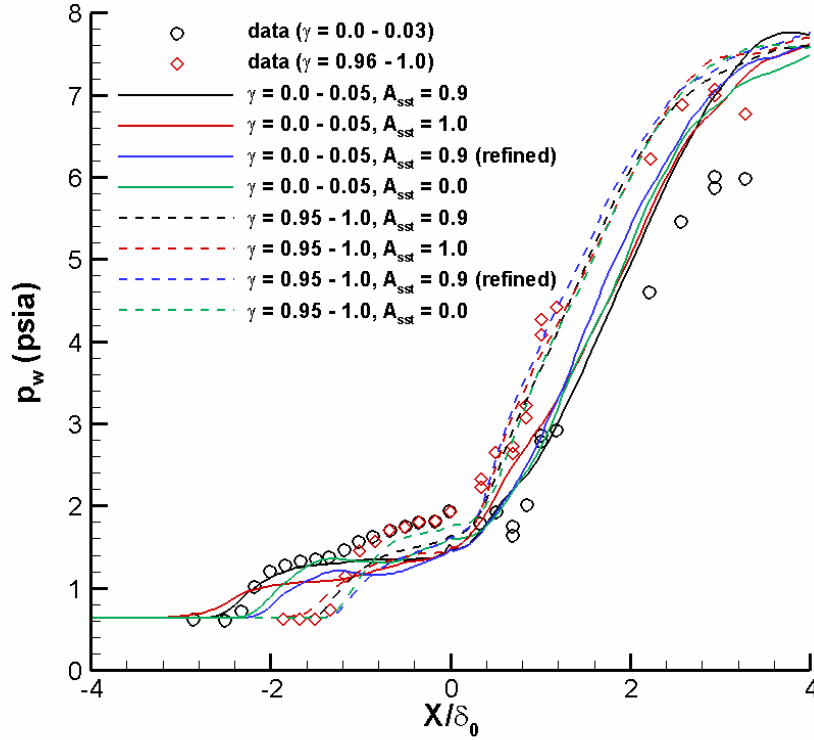


Figure 20: Conditionally-averaged surface pressure distributions

at all stations within the separation zone, there is at least a twenty-percent probability of having positive axial flow near the surface. In the region of separation-shock intermittency, the probability of reversed flow ranges from near zero at $\gamma = 0$ to 0.8 at $\gamma = 1$. From this, it can be concluded that the most downstream positioning of the separation shock is strong enough to immediately separate the boundary layer, while the separation shock at its most upstream location is weaker and does not immediately induce reversed flow. Further downstream, the probability of reversed flow decreases to a value of about 0.5 before increasing again to a value of 0.8 near the wedge apex. A non-zero probability of having reversed flow exists on the wedge surface past $X/\delta_0 = 2.0$. This is associated with the effect of the counter-rotating vortices discussed in Section 5.2 in moving fluid away from the surface.

Conditional pressure distributions may be obtained by ‘binning’ streamwise wall pressure traces according to the position of the separation shock. Figure 20 compares pressure distributions corresponding to $\gamma = 0$ to 0.05 (the most upstream positioning of the shock) and $\gamma = 0.95$ to 1.0 (the most downstream positioning) versus experimental data. Good agreement is generally achieved for the most downstream positioning of the separation shock, with the $A_{sst} = 0.0$ calculation providing the best prediction. The $A_{sst} = 1.0$ calculation correctly predicts the separation-shock position for the $\gamma = 0$ to 0.05 range, but the pressure level just upstream of the wedge apex is under-predicted and the pressure level on the ramp surface is over-predicted. These trends again relate to deficiencies in predicting the displacement effects of the separation bubble.

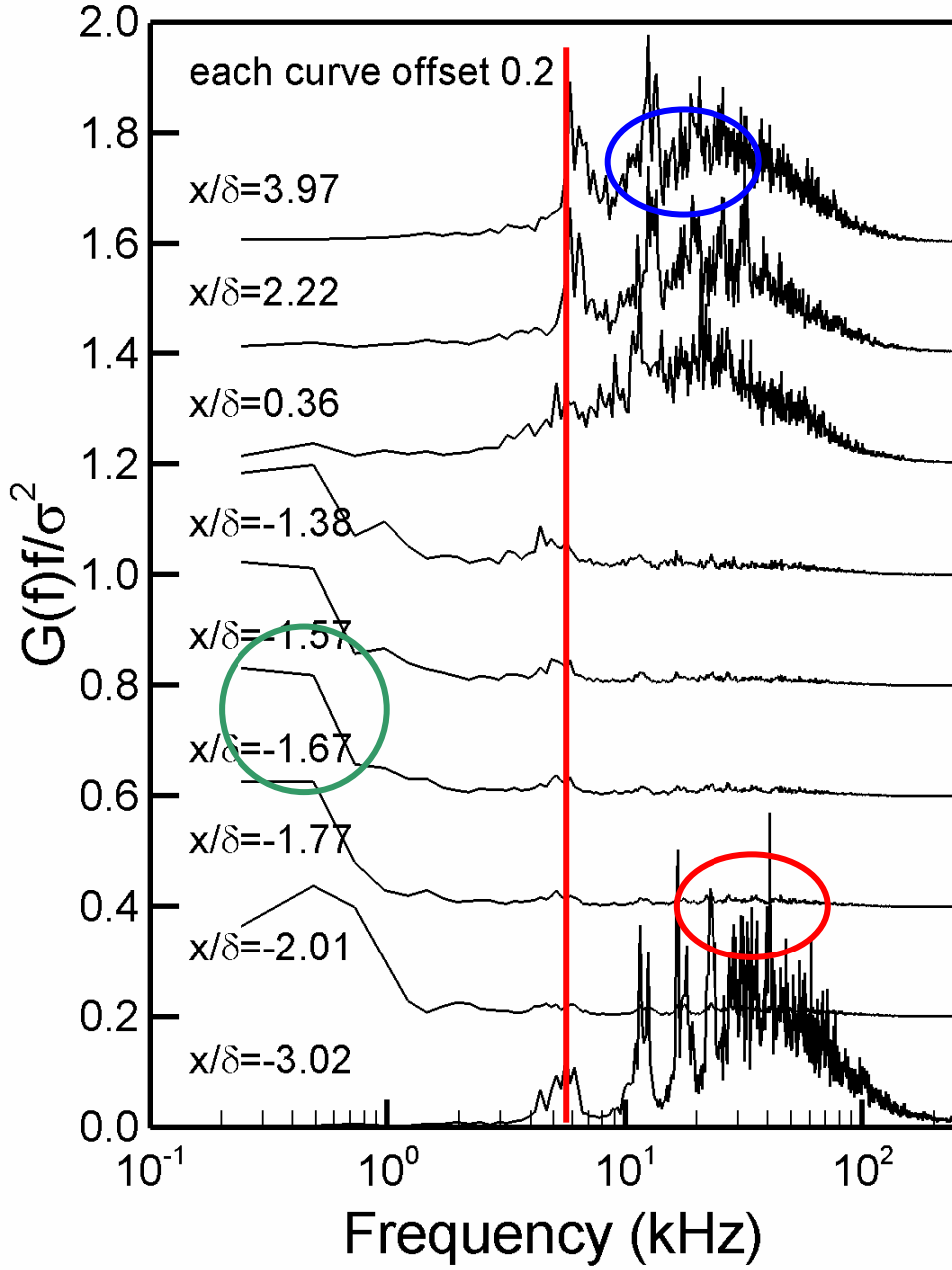


Figure 21: Power spectra at different streamwise stations

Figure 21 presents power spectra obtained at several X stations from pressure data extracted at $Y/\delta_0=0.2$. The $A_{sst}=0.9$ database on the baseline grid is used in these calculations; similar results are obtained for the other databases. As before, the ensemble of data in the interval $-1.8 < Z/\delta_0 < 1.8$ is used. Each power spectrum is normalized by the variance of the pressure signal and the frequency, as in [5]. Estimated large-eddy frequencies in the incoming boundary layer

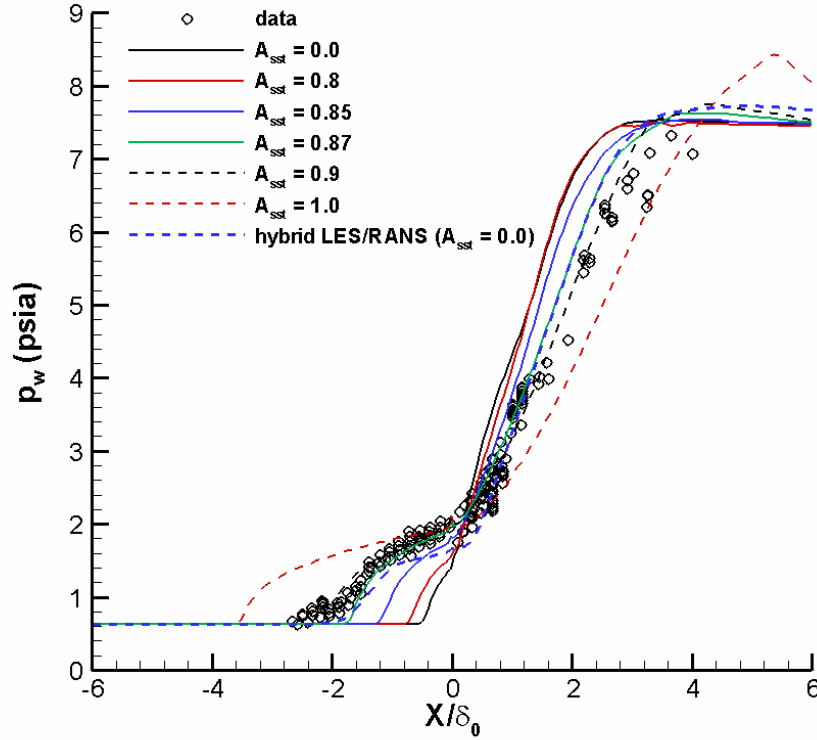


Figure 22: Wall pressure distributions (RANS models)

(based on δ_0 and u_∞) are on the order of 40-50 kHz. The spectrum at $X/\delta_0 = -3.02$ shows that the frequencies containing most of the energy content lie in the range from 15 kHz to 50 kHz. This is in good agreement with results reported in [5] (Figure 40 in that reference). For X stations in the intermittent region, the dominant frequencies are much lower: ~ 0.3 to 1 kHz. This is also in good agreement with the results of Gramann (Figure 55 in [5]) which show a dominant band of low-frequency tones ranging from ~ 0.2 kHz to 2 kHz. Downstream of the wedge apex, the lower-frequency tones diminish, and a higher frequency spectrum emerges. The dominant frequencies in the ramp boundary layer lie in the interval from ~ 8 to 30 kHz, which is in good agreement with Gramann's data (Figure 106 in [5]). The shift to lower frequencies (relative to those in the incoming boundary layer) may be attributed to the reduced convection speed of eddies downstream of the shock system, as the eddy sizes appear to be similar in the calculations. At all stations, a selection of tones with frequencies ranging from 5 to 7 kHz is seen. These appear to coincide with the recycling frequency, which is approximately equal to $u_\infty / (7\delta_0)$. This band of frequencies is not dominant at any location though its relative importance does appear to increase in the re-attachment / recovery region. Excepting the presence of the recycling frequency, the predictions are in close agreement with experimental observations, indicating that the hybrid LES/RANS model is capable of capturing both low and high-frequency dynamics of the interaction.

5.5. Comparisons with RANS Mean Flow Data

It is useful to compare predictions obtained by the baseline RANS model with those provided by the LES/RANS model. If the LES/RANS model can be proven more accurate, then it may be

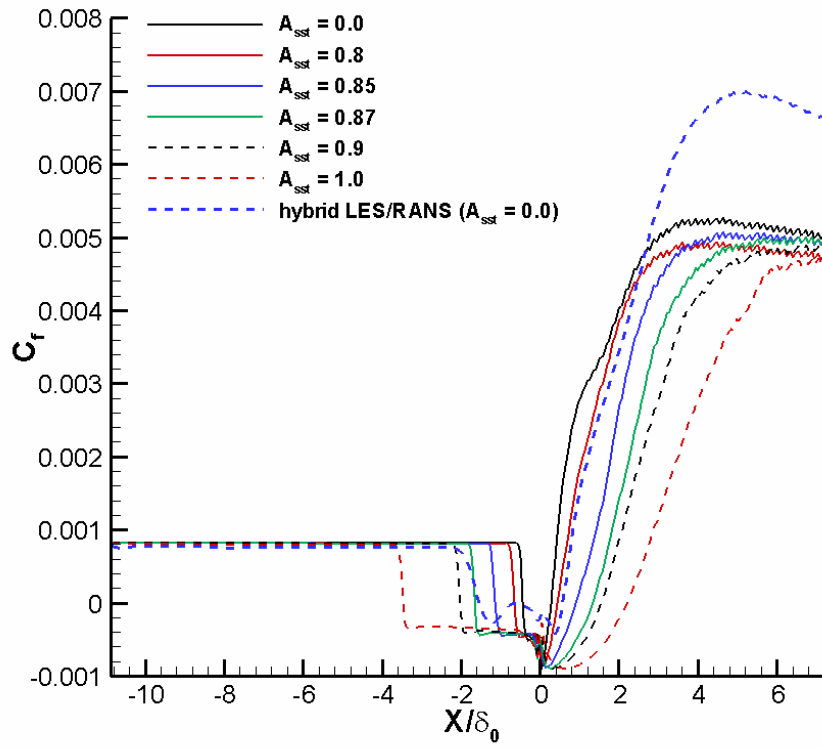


Figure 23: Skin friction distributions (RANS models)

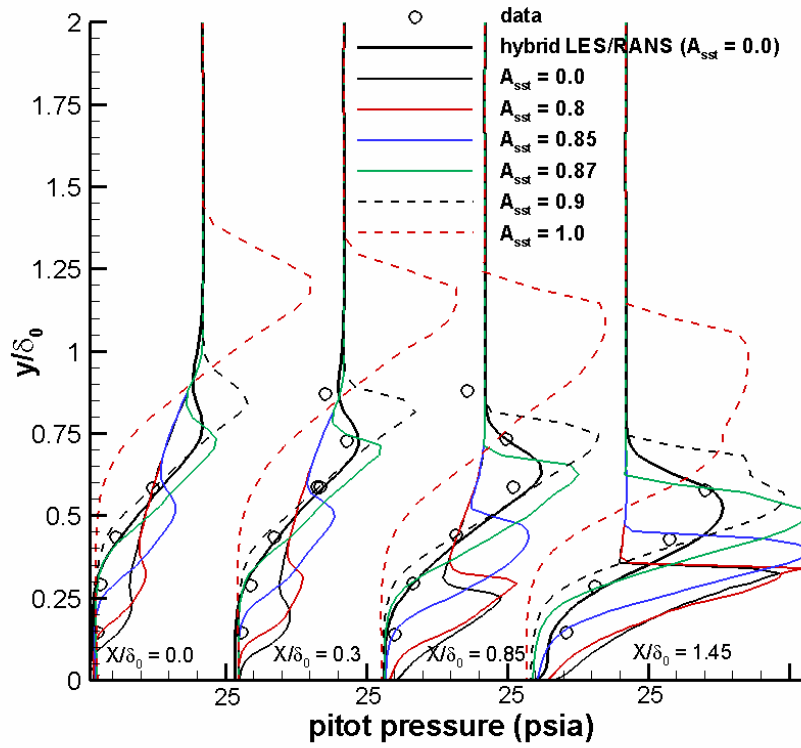


Figure 24: Pitot pressure profiles in re-attachment region (RANS models)

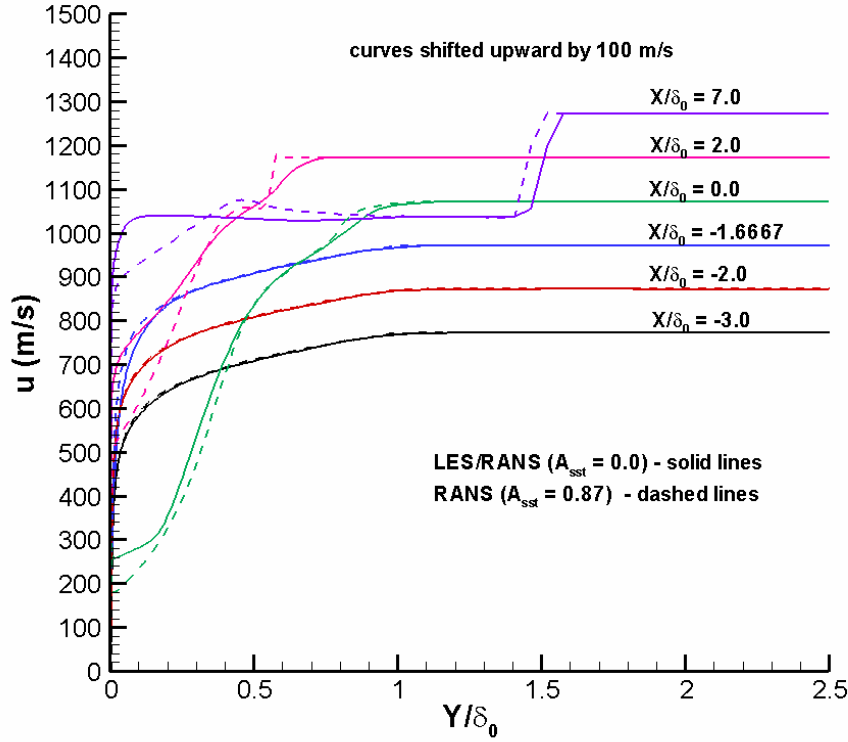


Figure 25: Axial velocity profiles throughout the interaction

possible to use LES/RANS data to evaluate modeled forms for various closure terms appearing in RANS models and from that, hopefully improve their predictive capability. Figure 22 shows the sensitivity of the wall pressure distributions predicted by the RANS model to the choice of the scaling constant A_{sst} . As noted, a value of $A_{sst} = 0.0$ results in the appearance of a small separation bubble, while the choice of $A_{sst} = 1.0$ results in a very large separation region. This level of sensitivity is much larger than that exhibited by the LES/RANS model (Figure 9). The best agreement with experimental data is achieved when A_{sst} is set to 0.9, while a value of $A_{sst} = 0.87$ provides a good comparison with the best LES/RANS prediction ($A_{sst} = 0.0$). Skin friction distributions in Figure 23 indicate that the RANS models consistently predict larger (in magnitude) near-wall velocities in the back flow region in comparison with the LES model. The RANS solutions also exhibit a delayed re-attachment and a slower rate of recovery in the inner layer, compared with the LES/RANS solution. Pitot pressure profiles shown in Figure 24 indicate that none of the RANS models predicts the experimental trends as closely as the LES/RANS model with $A_{sst} = 0.0$. The best agreement, not coincidentally, is provided by the $A_{sst} = 0.87$ RANS solution. Axial velocity profiles at different streamwise stations in Figure 25 reveal relatively close agreement between the $A_{sst} = 0.87$ RANS solution and the $A_{sst} = 0.0$ LES/RANS solution upstream of the wedge apex. However, the transport of momentum toward the surface in the re-attachment region ($X/\delta_0 = 2.0$) is clearly larger for the LES/RANS solution. The velocity profile further downstream ($X/\delta_0 = 7.0$) is fuller and flatter as a result, and the

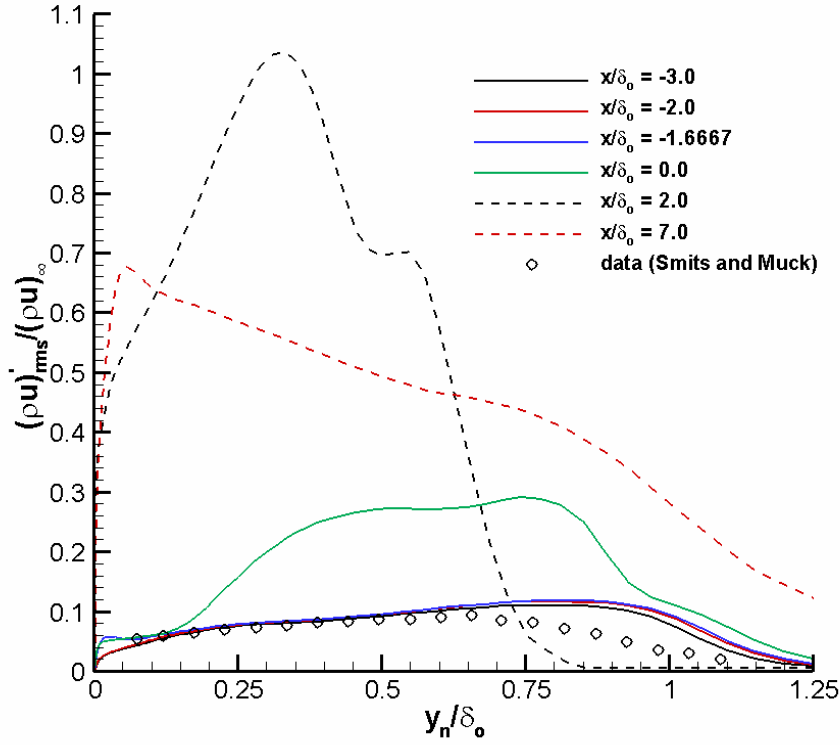


Figure 26: rms mass flux fluctuation profiles throughout the interaction

reduction in velocity due to wall shear is confined to a very thin layer near the surface. The velocity field does not return to an equilibrium profile within the extent of the domain for either model. In the absence of experimental data downstream of $X/\delta_o=2.0$, it is difficult to judge which approach might provide the more correct response, but other experimental studies at Mach 3 [30,31] have measured fuller, flatter boundary layer profiles in the recovery region. Moreover, earlier hybrid LES/RANS calculations [10-12] have been able to capture the experimental trends, whereas RANS models have not.

5.6. Comparisons with RANS Reynolds Stress Data

Figure 26 presents the evolution of *rms* mass flux fluctuation $\langle [(\rho u)']^2 \rangle^{1/2}$ profiles throughout the interaction region. Fluctuations are amplified by about a factor of 10 near the re-attachment position before reducing to a factor of about 7 near the end of the ramp. Maximum mass flux amplification factors of about 4 are reported for the Mach 3 experiments of Smits and Muck [27] and Zheltovodov, et al. [31] and for the computations of Loginov, et al. [14].

Contour plots of $\langle \rho k \rangle$, where k is the turbulence kinetic energy per unit mass, are shown in Figure 27 for the LES/RANS model with $A_{sst}=0.0$ and the RANS model with $A_{sst}=0.87$. Only the resolved-scale part of $\langle \rho k \rangle$ is presented for the LES/RANS model. The plots shows that

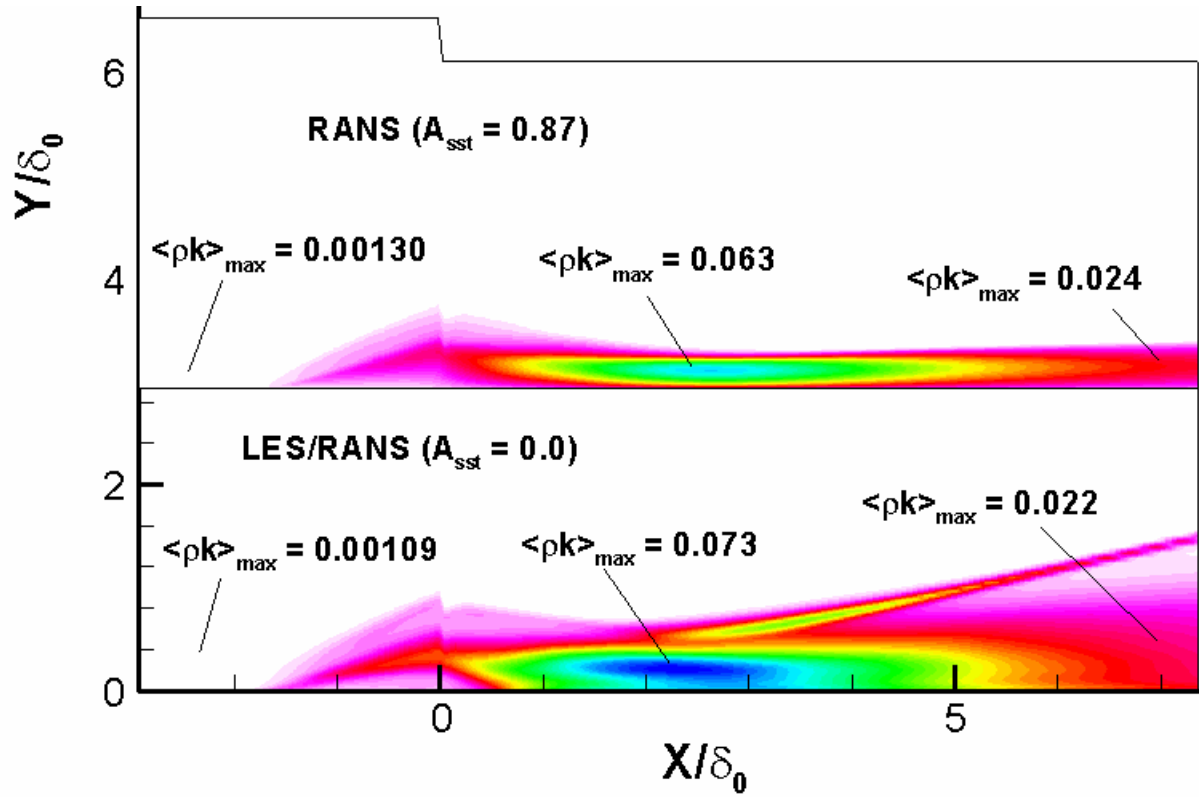


Figure 27: Contours of turbulence kinetic energy (normalized by $\rho_{\infty} u_{\infty}^2$)

amplification of the turbulence kinetic energy begins upstream of the wedge, with the maximum value in this region located within the shear layer that develops above the separation bubble. The turbulence amplification effect continues as the shear layer re-attaches, and the turbulence kinetic energy reaches its maximum value in the vicinity of the re-attachment shock. Clearly indicated in the LES/RANS results is the effect of the shock motion in enhancing the amplification rates and in broadening the turbulence kinetic energy distribution. Further downstream, the turbulence kinetic energy begins to decay, and the peak values near the end of the domain for the LES/RANS and RANS models are comparable. The distribution of turbulence kinetic energy in the normal direction is much wider for the LES/RANS calculation, and the peak is located well away from the surface. This may be due to convection of turbulence kinetic energy into the outer part of the recovering boundary layer, as the mean velocity gradient in this region is relatively small (Figure 25). The RANS result displays the expected trend of locating the maximum turbulence kinetic energy nearer the wall where the predicted mean velocity gradient is larger. The maximum amplification factor (relative to the turbulence kinetic energy level in the middle part of incoming boundary layer) is around 67 for the LES/RANS calculation and around 48 for the RANS calculation. The amplification factors reduce to 20 and 18 for the LES/RANS and RANS calculations, respectively, toward the end of the ramp. These values are much larger than the eight-fold amplification observed in the Mach 3 experiments of Smits and Muck [27] for the Reynolds normal stress. In the Mach 3 experiments, the compression fan that forms downstream of the re-attachment position does not coalesce into a shock within the boundary layer, whereas in the Mach 5 calculations (and probably in the experiment), the coalescence of the compression fan into a shock takes place close to the wall, and the coalesced shock interacts dynamically with the re-attaching shear layer.

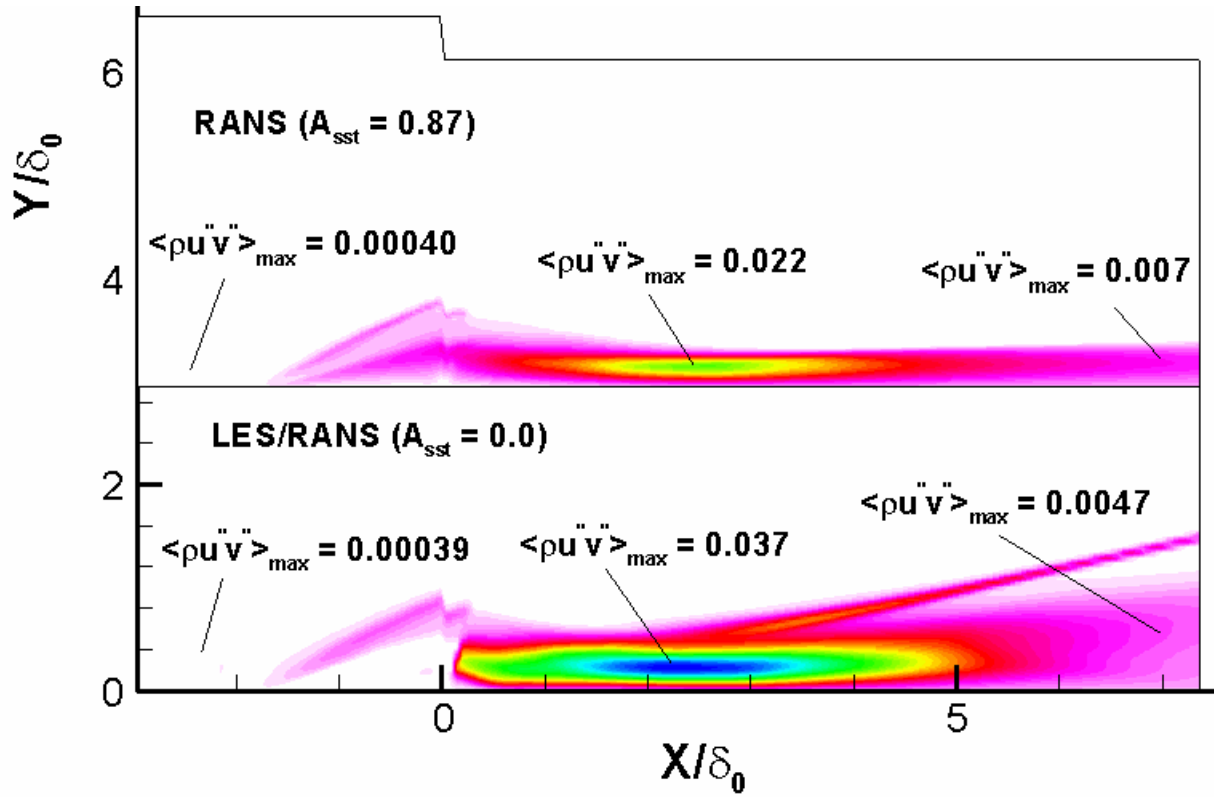


Figure 28: Contours of Reynolds shear stress (normalized by $\rho_\infty u_\infty^2$)

Contours of the Reynolds shear stress $\langle \rho u'v' \rangle$ are shown in Figure 28. The Reynolds stress tensor is rotated so that the shear component is tangential to the surface. Upstream of the wedge apex, the LES/RANS model predicts the maximum value of the shear stress as occurring toward the outer edge of the separating shear layer, whereas the separation region is associated with small values of the Reynolds shear stress. The RANS model displays the expected trend of a maximum Reynolds shear stress where the velocity gradient is largest. Downstream of the wedge apex, the trends generally follow that evidenced for the turbulence kinetic energy. The maximum amplification factors are even larger: 95 for the LES/RANS calculation and 55 for the RANS calculation. These reduce to factors of 12.5 and 17.5 for the LES/RANS and RANS calculations near the end of the ramp. Loginov, et al. [14] report a maximum Reynolds shear stress amplification of 28 in their calculations. The structure factor $\langle \rho u'v' \rangle / \langle \rho k \rangle$, evaluated at the location of maximum Reynolds shear stress toward the end of the ramp, is about 0.265 for both models, indicating that both computed boundary layers may be returning toward equilibrium but through different paths. The locations of the maximum Reynolds shear stress differ significantly, with the LES/RANS calculation placing this location further away from the wall than the RANS calculation. Additional experimental data would be required to determine which modeling approach best captures the evolution of the Reynolds stress tensor for this flow.

6. Conclusions

Simulations of a Mach 5 compression-corner interaction at $Re/m = 50.1e6$ have been performed using a hybrid large-eddy / Reynolds averaged Navier-Stokes (LES/RANS) model. The model

uses a flow-dependent blending function to shift the closure from Menter's two-equation RANS model near walls to a Smagorinsky subgrid closure model in the outer part of the boundary layer. The blending function is based on a modeled form of the Taylor microscale and is designed to transition to LES toward the outer part of the logarithmic region (for equilibrium boundary layers). A recycling / rescaling technique, applied to the fluctuating fields, is used to initiate and sustain large-eddy motion. The following conclusions may be stated.

1. The LES/RANS models capture the mean-flow and time-dependent structure of the interaction reasonably well. Observed deficiencies relate primarily to an under-prediction of the size of the separation region (particularly its vertical extent), which causes a smaller separation-shock pressure rise and a larger re-attachment shock pressure rise than observed experimentally.
2. The LES/RANS results are sensitive to the amount of 'shear stress transport' (SST) included in the Menter model – the calculations performed without the SST modification are in better agreement with experimental data. Inclusion of the SST effect improves predictions of the upstream influence of the shock system but reduces the vertical displacement of the separation region. The separation shock pressure rise is lessened and its dynamics not as vigorous as a result.
3. In accord with recent LES results at Mach 3 [14], the current work predicts significant three-dimensional effects in the time-averaged flow downstream of the re-attachment position. These appear to relate to the formation of counter-rotating vortex pairs in the re-attaching boundary layer. The positions of these vortical structures do not migrate substantially over the time intervals considered.
4. Recent conjectures [8] relating to the development of a low-frequency motion of the entire shock system due to the persistence of streaks of fluid with lower or higher momentum than the average are supported by the current simulations. In the simulations, it appears to be the collective effect of several neighboring streaks that induces a low-frequency undulation in the separation-shock front. The passage of individual streaks of fluid through the front produces localized ripples but not large-scale motion.
5. The dynamics of the shock-system motion, as quantified by conditional pressure distributions, shock-position intermittency distributions, and power spectra analysis at different locations, have been predicted to good accord by the LES/RANS model. The use of a RANS component near the surface does appear to mitigate the near-wall dynamics of the separation shock to some degree. Upon re-attachment, however, the RANS region is forced closer to the wall, and there are indications that the model may not provide enough damping of large-scale fluctuations in this region.
6. Calculations performed using the baseline Menter RANS model are much more sensitive to the amount of 'shear stress transport' included. The RANS calculations also predict re-attachment as occurring further downstream than seen in the experiment or in the LES/RANS predictions, and the rate of recovery of the boundary layer in the near-wall region is not as rapid as observed in the LES/ RANS models or in the experimental results available. Both models predict substantial amplification of Reynolds normal and shear stresses downstream of re-attachment, but the distribution of the Reynolds stresses within the boundary layer is much broader for the LES/RANS model. This effect appears to be due to re-attachment shock motion.

7. From a perspective of improving RANS models for this type of flow, it is clear that nominally two-dimensional flow might not be attained downstream of the re-attachment line. This means that two-dimensional RANS models must account for the collective effects of pairs of counter-rotating vortices, and it is unclear what average state one might expect to predict. This fact might explain why RANS models, even if tuned to capture the separation-shock location, inevitably fail to capture the correct recovery rate of the boundary layer downstream of re-attachment.

7. Directions for Future Work

There are several remaining sources of uncertainty in the application of hybrid LES/RANS models to strongly-interacting, wall-bounded flows. These comprise directions for future work and are summarized as follows.

1. The over-prediction of the Reynolds stress in the outer part of the incoming boundary layer (Figure 3) is a cause for concern, assuming that the Smits / Muck database is accurate enough to be used as a benchmark. We believe that this effect might result from a small inconsistency in how the recycling / rescaling method is being applied, and we will test some modifications designed to correct this.
2. The collapse of the blending function (and thus the removal of much of the RANS component of the closure) downstream of re-attachment is also an issue in that the expected dissipative effects of near-wall eddies may not be modeled properly. We have also observed this effect in simulations of a Mach 8 crossing-shock interaction. [13]. We are modeling the response of the blending functions and LES/RANS turbulence models using RANS mean data in an attempt to determine how these models return to equilibrium. Insights gained in this study may point toward improvements in the blending function approach.
3. The impact of the numerical discretization on the separation-shock position is uncertain. Calculations (not shown) using our earlier Sonic-A ENO schemes inevitably over-predicted the extent of the separation region, while the PPM calculations presented herein slightly under-predicted the size of the separation region. The capturing of the separation-shock pressure rise might be improved by modifying the limiting procedure in Eq. 2.
4. We have not yet attempted to use a more sophisticated subgrid closure in these calculations. Some candidates include structure-function models and localized dynamic models, as well as models that rely on an equation for the subgrid turbulence kinetic energy. Our earlier work used Yoshizawa's model [33] in this context, but we really haven't seen a definite benefit from using a one-equation subgrid model versus an algebraic model.
5. It appears that predicting the structure of the flow in the re-attachment / recovery region may be the most uncertain aspect. It would be useful to re-consider experimental databases that provide more data in this region. Some candidates include the Mach 3 Smits and Muck database (and the earlier work by Settles and Bogdanoff [31]). The pioneering study of Dolling and Murphy [34] also corresponds to these compression-corner experiments, so there is data available on shock-system dynamics.

6. An investigation of shock motion effects as induced by three-dimensional interactions (sharp fins) may also be worthwhile.

Publications

Edwards, J.R., Choi, J-I., and Boles, J.A. "Hybrid LES/RANS Simulation of a Mach 5 Compression-Corner Interaction" Abstract submitted for presentation at the 46th Aerospace Sciences Meeting, January, 2008. We also plan to submit a version to *AIAA Journal*.

Boles, J.A. "Hybrid LES/RANS Simulation of a 10-degree Double Fin Crossing Shock Flow at Mach 8.28" M.S. Thesis, North Carolina State University, February, 2007.

Edwards, J.R. "Simulation of Transient Dynamics of Shock Wave / Boundary Layer Interactions using Hybrid Large-Eddy / Reynolds-Averaged Navier-Stokes Models" Final Technical Report, U.S. Army STIR Grant W911NF-06-1-0299, May, 2007

Personnel

Jack R. Edwards, Principal Investigator

Jung-II Choi, Post-Doctoral Research Associate (responsible for performing the power spectra analysis)

John A. Boles, Graduate Research Assistant (completed his M.S. Thesis, entitled "Hybrid LES/RANS Simulation of a 10-degree Double Fin Crossing Shock Flow at Mach 8.28" in February, 2007)

Most of the ARO support was used to fund John Boles in completing his M.S. degree in Aerospace Engineering.. As John had already been working on his thesis project for over a year, it was decided to allow him to spend the majority of his time completing this work. John is now a Ph.D candidate at NCSU. The work outlined in the proposal was performed primarily by Dr. Edwards, assisted by Dr. Choi.

Bibliography

- [1] Dolling, D.S., "Fifty Years of Shock Wave / Boundary-Layer Interaction Research: What Next?" *AIAA Journal*, Vol. 39, No. 8, 2001, pp. 1517-1531.
- [2] Marshall, T.A. and Dolling, D.S. "Computation of Turbulent, Separated, Unswept Compression Ramp Interactions", *AIAA Journal*, Vol. 30, No. 8, 1992, pp. 2056-2065.
- [3] Dolling, D.S. "High-Speed Turbulent Separated Flows: Consistency of Mathematical Models and Flow Physics", *AIAA Journal*, Vol. 36, No. 5, 1998, pp. 725-732.
- [4] McClure, W.B. and Dolling, D.S. "Exploratory Study of Effects of Suction Near Reattachment on the Unsteadiness of a Mach 5 Compression Ramp Interaction", AIAA Paper 91-1767, June, 1991.
- [5] Gramann, R. A. "Dynamics of Separation and Reattachment in a Mach 5 Unswept Compression Ramp Flow," Ph.D. Dissertation, Dept. of Aerospace Engineering and Engineering Mechanics, University of Texas, Austin, TX, 1989.

- [6] Erengil, M.E. and Dolling, D.S. "Separation Shock Motion and Ensemble-Averaged Wall Pressures in a Mach 5 Compression Ramp Interaction", *AIAA Journal*, Vol. 29, No.5, 1991, pp.728-735.
- [7] Beresh, S.J. Clemens, N.T., and Dolling, D.S. "Relationship between upstream turbulent boundary-layer velocity fluctuations and separation shock unsteadiness" *AIAA Journal*, Vol. 40, No. 12, 2002, pp. 2412-2422.
- [8] Ganapathisubramani, B., Clemens, N.T., and Dolling, D.S. "Planar Imaging Measurements to Study the Effect of Spanwise Structure of Upstream Turbulent Boundary Layer on Shock-Induced Separation" AIAA Paper 2006-0324, January, 2006.
- [9] Baurle, R.A., Tam, J., Edwards, J.R., and Hassan, H.A. "Hybrid RANS/LES Approach for Cavity Flows: Blending, Algorithm, and Boundary Treatment Issues" *AIAA Journal*, Vol. 41, No. 8, 2003, pp. 1463-1480.
- [10] Xiao, X., Edwards, J.R., Hassan, H.A., and Baurle, R.A. "Inflow Boundary Conditions for Hybrid Large-Eddy / Reynolds-Averaged Navier-Stokes Simulations" *AIAA Journal*, Vol. 41, No. 8, 2003, pp. 1481-1490.
- [11] Fan, T.C., Edwards, J.R., Hassan, H.A., and Baurle, R.A. "Hybrid Large-Eddy / Reynolds-Averaged Navier-Stokes Simulations of Shock-Separated Flows," *Journal of Spacecraft and Rockets*, Vol. 41, No. 6, pp.897-906.
- [12] Xiao, X., Edwards, J.R., and Hassan, H.A. "Blending Functions in Hybrid Large-Eddy / Reynolds-Averaged Navier-Stokes Simulations," *AIAA Journal*, Vol. 42, No. 12, pp. 2508-2515.
- [13] Boles, J.A. and Edwards, J.R. "Hybrid Large-Eddy / Reynolds-Averaged Navier-Stokes Simulation of a Mach 8.3 Crossing-Shock Interaction," AIAA Paper 2006-3039, June, 2006. \
- [14] Loginov, M.S., Adams, N.A., and Zheltovodov, A.A. "Large Eddy Simulation of Shock-Wave / Turbulent-Boundary-Layer Interaction" *Journal of Fluid Mechanics*, Vol. 565, 2006, pp. 135-169.
- [15] Wu, M. and Martin, M.P. "Direct Numerical Simulation of Supersonic Turbulent Boundary Layer over a Compression Ramp" *AIAA Journal*, Vol. 45, No. 4, 2007, pp. 879-889.
- [16] Hunt, D., and Nixon, D. "A Very Large Eddy Simulation of an Unsteady Shock Wave / Turbulent Boundary Layer Interaction" AIAA Paper 95-2122, June, 1995.
- [17] Roy, C.J. and Edwards, J.R. "Numerical Simulation of a Three-Dimensional Flame / Shock Wave Interaction," *AIAA Journal*, Vol. 38, No. 5, 2000, pp. 745-760.
- [18] Edwards, J.R. "A Low-Diffusion Flux-Splitting Scheme for Navier-Stokes Calculations," *Computers Fluids*, Vol. 26, No. 6, 1997, pp. 635-659.
- [19] Colella, P. and Woodward, P.R. "The Piecewise Parabolic Method (PPM) for Gas-Dynamical Simulations", *Journal of Computational Physics*, Vol. 54, pp. 174-201, 1984
- [20] Suresh, A. and Huynh, H.T. "Numerical Experiments on a New Class of Non-Oscillatory Schemes," AIAA Paper 92-0421, Jan. 1992.
- [21] Menter, F.R. "Two Equation Eddy Viscosity Turbulence Models for Engineering Applications," *AIAA Journal*, Vol. 32, No. 8, 1994, pp. 1598-1605.
- [22] Strelets, M., "Detached Eddy Simulation of Massively Separated Flows," AIAA Paper 2001-0879
- [23] Walz, A. Boundary Layers of Flow and Temperature (English translation), MIT Press, 1969.
- [24] Wilcox, D. C., Turbulence Modeling for CFD, DCW Industries, 2nd ed., 1998.
- [25] Tomioka, S., Jacobsen, L.S., and Schetz, J.A. "Sonic Injection from Diamond-Shaped Orifices into a Supersonic Crossflow", *Journal of Propulsion and Power*, Vol. 19, No. 1, 2003, pp. 104-114.

- [26] Wu, M., Bookey, P., Martin, M.P., and Smits, A.J. "Analysis of Shockwave / Turbulent Boundary Layer Interaction using DNS and Experimental Data", AIAA Paper 2006-6310, January, 2005.
- [27] Smits, A.J. and Muck, K-C. "Experimental Study of Three Shock-Wave / Turbulent Boundary Layer Interactions" *Journal of Fluid Mechanics*, Vol 192, 1987, pp. 291-314.
- [28] Zheltovodov, A.A., Schulein, E., and Yakovlev, V.N., Development of Turbulent Boundary Layers Under Conditions of Mixed Interaction with Shock and Expansion Waves", Preprint 28-83, ITAM, USSR Academy of Sciences, Siberian Branch, Novosibirsk (in Russian)
- [29] Navarro-Martinez, S., and Tutty, O.R. "Numerical Simulation of Görtler Vortices in Hypersonic Compression Ramps" *Computers and Fluids*, Vol. 34, 2005, pp. 225-247.
- [30] http://www.ae.utexas.edu/research/FloImLab/inst_bl.gif
- [31] Settles, G.S., and Dodson, L.J. "Hypersonic Shock / Boundary Layer Interaction Database," NASA CR-177577, April, 1991.
- [32] Zheltovodov, A. A., Zaulichnii, E. G., Trofimov, V. M., and Yakolev, V. N "Heat Transfer and Turbulence Study in Compressible Separated Flows" Preprint 22-87, Inst. Theoretical and Applied Mechanics, Russian Academy of Sciences, Novosibirsk, 1987.
- [33] Yoshizawa, A. and Horiuti, K. "A Statistically-Derived Subgrid Scale Kinetic Energy Model for Large-Eddy Simulation of Turbulent Flows," *Journal of the Physical Society of Japan*, Vol. 54, 1985, p. 2834.
- [34] Dolling, D.S. and Murphy, M.T. "Unsteadiness of the Separation Shock-Wave Structure in a Supersonic Compression Ramp Flowfield" *AIAA Journal*, Vol. 21, No. 12, 1983, pp. 1628-1634.

Appendices

The following material is included as a supplement to this report.

- 1.) PDF file containing John Boles' Master of Science thesis
- 2.) Powerpoint file containing a presentation given at ARO on May 4, 2007, along with associated animations.